nature materials

Article

https://doi.org/10.1038/s41563-022-01414-y

Topological steering of light by nematic vortices and analogy to cosmic strings

Received: 11 December 2021

Accepted: 18 October 2022

Published online: 1 December 2022

Check for updates

Cuiling Meng[1,5], Jin-Sheng Wu[1,5] & Ivan I. Smalyukh[1,2,3,4]

Liquid crystals are widely known for their technological uses in displays, electro-optics, photonics and nonlinear optics, but these applications typically rely on defining and switching non-topological spatial patterns of the optical axis. Here, we demonstrate how a liquid crystal's optical axis patterns with singular vortex lines can robustly steer beams of light. External stimuli, including an electric field and light itself, allow us to reconfigure these unusual light–matter interactions. Periodic arrays of vortices obtained by photo-patterning enable the vortex-mediated fission of optical solitons, yielding their lightning-like propagation patterns. Predesigned patterns and spatial trajectories of vortex lines in high-birefringence liquid crystals can steer light into closed loops or even knots. Our vortex lattices might find technological uses in beam steering, telecommunications, virtual reality implementations and anticounterfeiting, as well as possibly offering a model system for probing the interaction of light with defects, including the theoretically predicted, imagination-capturing light-steering action of cosmic strings, elusive defects in cosmology.

Liquid crystals (LCs) combine the anisotropic optical properties and facile responses to external stimuli that are characteristic for these soft matter systems[1]. The average LC rodlike molecular alignment direction, the director, has non-polar symmetry $\mathbf{n} \equiv -\mathbf{n}$ and is also the optical axis. Optical properties of the most common nematic LCs are analogous to those of solid uniaxial crystals, with the propagation of ordinary and extraordinary modes of light dependent on the optical axis orientation[1]. However, unlike in solid crystals, the optical axis (director) field $\mathbf{n}(\mathbf{r})$ can adopt complex spatial configurations, varying with spatial coordinates $\mathbf{r}$ [2], and can exhibit facile switching. This combination of physical properties enables widespread technological applications of LCs, ranging from displays to nonlinear optics[1,3,4], which typically exploit various reorientations of the optical axis in response to applied fields or light itself. Although topology can define the material properties and behaviour of physical systems[2], its role in enriching the control of light by LCs, such as in non-mechanical laser beam steering, remains unexplored as the existing applications typically rely on defining and switching non-topological spatial patterns of the optical axis. LCs also offer a facile formation of topological defects[2], fascinating structural diversity, rich phase behaviour and physical properties that allow them to be used as model systems in studies of topology-related effects in other physical systems[2,5–20]. However, due to the quick annihilation of LC vortices after the isotropic–nematic phase transition and strong light scattering in the nematic medium caused by LC director fluctuations[7], the interaction of light with the vortex-containing patterns of the optical axis has never been probed experimentally, to the best of our knowledge. The technological potential of LCs with controlled patterns of vortices could not be tested or utilized until now.

Here we define configurations of vortex lines stretched across the nematic LC bulk by a microscale surface photo-patterning of the LC director alignment that was recently used in controlling colloids, bacteria and networks[8,21–23]. This patterning of surface boundary conditions pins LC vortices in desired spatial locations and precludes their annihilation. We then generate optical solitons to form non-spreading light valves that robustly traverse our LC with vortices. The ensuing light–defect interactions are understood based on the Fermat

[1]Department of Physics and Chemical Physics Program, University of Colorado, Boulder, CO, USA. [2]Materials Science and Engineering Program, University of Colorado, Boulder, CO, USA. [3]International Institute for Sustainability with Knotted Chiral Meta Matter, Hiroshima University, Higashihiroshima, Japan. [4]Renewable and Sustainable Energy Institute, National Renewable Energy Laboratory and University of Colorado, Boulder, CO, USA. [5]These authors contributed equally: Cuiling Meng, Jin-Sheng Wu. e-mail: ivan.smalyukh@colorado.edu

https://doi.org/10.1038/s41563-022-01414-y

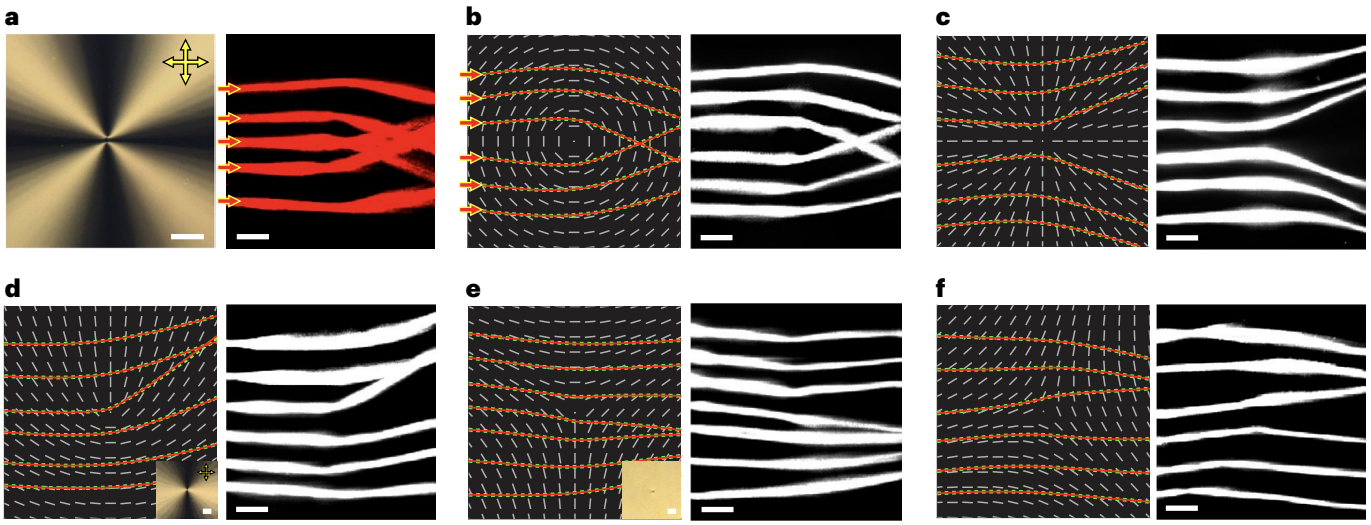

Fig. 1 | Topological steering of light by LC vortices. a, Polarizing optical micrograph of a $k = 1$, $\Psi_0 = \pi/2$ vortex (left), obtained between crossed polarizers (double yellow arrows), and the corresponding deflection (right) of 650 nm laser beams incident parallel to the horizontal edge of the image from its left side (red arrows with yellow frame). **b**–**f**, Comparison of (left) computer-simulated light trajectories (red and dashed green lines), overlaid on top of corresponding $\mathbf{n}(\mathbf{r})$ (white cylinders), with (right) experimental optical soliton trajectories generated by 1,064 nm laser beams for defects with $k = 1$, $\Psi_0 = \pi/2$ (**b**); $k = 1$, $\Psi_0 = 0$ (**c**); $k = 1/2$, $\Psi_0 = \pi/4$ (**d**); $k = -1/2$, $\Psi_0 = \pi/4$ (**e**) and $k = -1/2$, $\Psi_0 = 5\pi/8$ (**f**). The insets in **d** and **e** show polarizing and bright-field optical micrographs of the corresponding vortices, which are the points where dark and bright brushes meet and where the dark dots associated with light scattering from the defect's core appear, respectively; note that the $k = 1$ defects locally split into two $k = 1/2$ ones. Closely matching computer-simulated red (dashed green) beam propagation trajectories are obtained by using Hamiltonian (Lagrangian) approaches (Methods). All scale bars are 100 μm.

principle, stating that the spatial trajectory of light propagation in all media is the one travelled within the shortest amount of time[24]. While optical nonlinearities enable the very formation of our optical solitons, also called 'nematicons'[25–27], these nonlinearities are weak, and linear approximation robustly describes how the topological defects steer the solitonic light[28]. Using azobenzene-based photo-responsive alignment layers and the coupling of the dielectric LC medium with applied electric fields[7,8,21], we show how this physical behaviour can be robustly controlled and reconfigured with external stimuli for wide-angle beam steering and light localization within closed loops or knots. We foresee that our topological steering of light could find technological uses in telecommunications, virtual reality designs, anticounterfeiting, nanophotonics and light-based energy storage.

Topological design and light steering by LC vortices

Uncontrolled geometric configurations and fast annihilation of vortices after the isotropic-to-nematic phase transition complicate experimental studies of light-vortex interactions. To overcome this challenge, we set the predesigned patterns of boundary conditions for azimuthal orientations of $\mathbf{n}(\mathbf{r})$ on the inner surfaces of confining glass plates using photo-patterned azobenzene dye. The azimuthal orientations of LC molecules and $\mathbf{n}(\mathbf{r})$ parallel to the confining glass substrates are controlled by the adjacent rodlike dye orientations, which, in turn, are controlled by the polarization of photo-patterning light (Extended Data Fig. 1). The photo-patterned two-dimensional defects in the rodlike dye orientations pin the ends of the bulk LC vortices with quasi-two-dimensional, translationally invariant $\mathbf{n}(\mathbf{r})$ structures in desired locations upon quenching from the isotropic phase, allowing for a microscopic view perspective along the vortex line and the geometry ideal for observing light–vortex interactions (Figs. 1 and 2). However, the LC medium normally causes strong light scattering[2,7] due to thermal fluctuations of $\mathbf{n}(\mathbf{r})$. To suppress this loss and extend light propagation, we tune the laser beam power to induce non-spreading optical solitons traversing the LC medium in a plane orthogonal to the vortex lines (Fig. 2 and Supplementary Notes). The residual out-of-plane light scattering from the optical solitons allows for experimental tracing of their propagation trajectories relative to the vortices imaged by polarizing optical microscopy (Figs. 1 and 2). The local reorientation of $\mathbf{n}(\mathbf{r})$ during nematicon generation and propagation is estimated to be within 0.001–0.01 rad, consistent with the literature and depending on the laser powers[25,28], which is sufficiently small for the purpose of justifying our linear approximation approach in the numerical ray tracing of light propagation within the LC.

Our design of individual vortices relies on an ansatz for the azimuthal azobenzene dye molecular orientations, with function $\Psi(y,x) = k\tan^{-1}(y/x) + \Psi_0$ defining the azimuthal angle of $\mathbf{n}(\mathbf{r})$, where k is the winding number describing the accumulated angle of $\mathbf{n}(\mathbf{r})$ rotation as one circumnavigates the vortex once, divided by 360°, y and x are cartesian coordinates, and Ψ_0 is the initial azimuthal angle. Optical micrographs obtained under crossed polarizers (examples in Fig. 1a, inset of Fig. 1d and Supplementary Video 1) are consistent with the quasi-two-dimensional $\mathbf{n}(\mathbf{r})$ fields of defects for different k and Ψ_0 values. By overlaying the optical soliton trajectories corresponding to different entry positions relative to the vortex lines, we vividly demonstrate how these defects cause bending of light (Fig. 1). Angular deflections behave discontinuously when light passes through a defect's core (Fig. 1) and are boosted by increasing optical ainisotropy Δn (Extended Data Fig. 2), where Δn is the difference between the LC's extraordinary n_e and ordinary n_o refractive indices.

Light guiding depends on the LC vortex's geometry, defined by k and Ψ_0. For example, axisymmetric $k = 1$ vortices cause convergence (divergence) for $\Psi_0 = \pi/2$ ($\Psi_0 = 0$) of incident parallel beams (Fig. 1a–c), where the light propagation trajectories on the opposite sides of vortices are mirror reflections of each other for both $k = 1$ vortices. The incident beams can also experience asymmetric deflections (Fig. 1d–f and Extended Data Fig. 3) when interacting with half-integer and other non-axisymmetric vortices, depending on the orientation of the symmetry planes characterizing $\mathbf{n}(\mathbf{r})$ relative to the incident light's propagation direction. The steering power of vortices increases with k,

https://doi.org/10.1038/s41563-022-01414-y

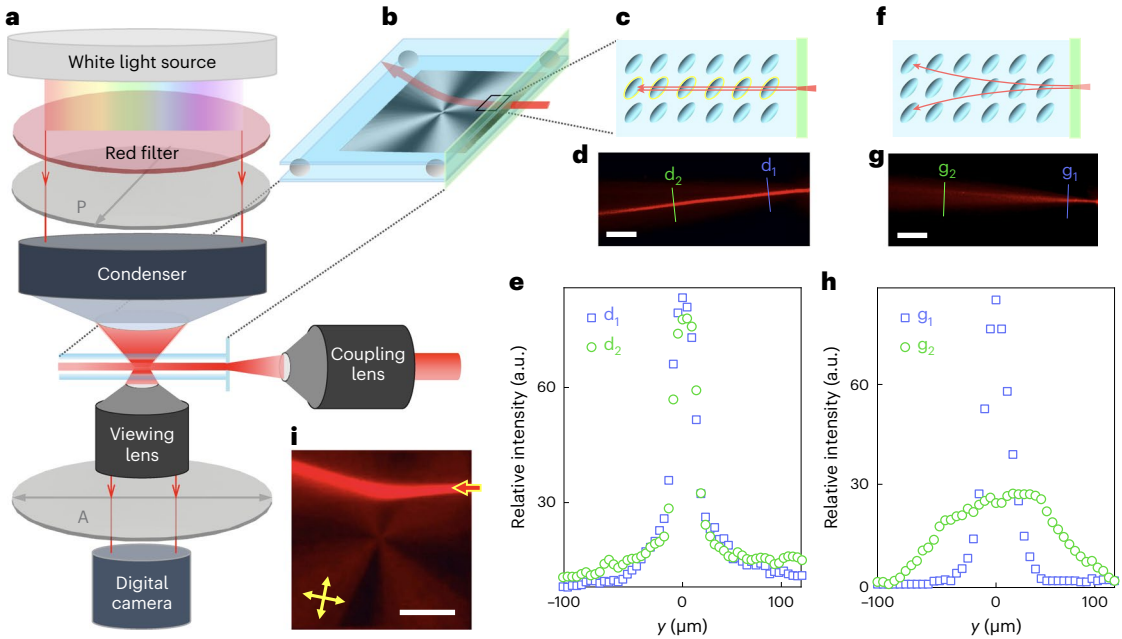

Fig. 2 | Launching of optical solitons into a cell with LC vortices. a, Schematic of a microscope, where a white-light source is filtered to let only red imaging light go through. Polarizer (P) and analyser (A) orientations are shown with double arrows. The red filter precludes the unwanted effects of imaging light on the azobenzene dye layers used for photo-patterning of the boundary conditions for $\mathbf{n}(\mathbf{r})$. **b**, A schematic showing a Gaussian laser beam (red arrow) launched into the LC cell to probe light–vortex interactions (not to scale). **c**,**f**, Schematic of self-focusing solitonic (**c**) and spreading (**f**) light beam traversing LC cells. **d**,**g**, Corresponding optical soliton (**d**) and conventional beam (**g**) obtained by launching 650 nm laser beams of powers 12 mW and 4 mW, respectively. **e**,**h**, Transverse relative intensity profiles along the lines d_1 and d_2 in **d** and g_1 and g_2 in **g** as functions of y (orthogonal to the beam). **i**, Beam trajectory overlayed (shown by red arrow) on top of a polarizing optical micrograph of a vortex with $k = 1$ and $\Psi_0 = 0$, corresponding to **b**. Double yellow arrows mark the orientations of the crossed polarizers. All scale bars are 200 μm.

as revealed for defects with $k = 3, 4, 6$ and 9 and their dimers (Extended Data Figs. 4 and 5). By shifting beams relative to these vortices, light trajectories can be dynamically reconfigured (Supplementary Video 2).

Experimental trajectories of optical solitons in LCs are fully reproduced by two different types of modelling (Fig. 1, Extended Data Figs. 3–5 and Methods). The Lagrangian-based modelling exploits the geodesic equation in an effective geometry, as originally introduced for cosmic strings and later adopted for theoretical predictions of light interactions with vortices in nematic LCs[14–18], and is consistent with the Hamiltonian ray-tracing method recently used for modelling LC media[28]. The observed light–matter interactions result from the effective geometry seen by light, which in the Euclidean space can be interpreted as a geodesic (Methods), showing a striking similarity of light-steering effects due to $k = 1$ LC defects and those expected for elementary cosmic strings[29–35], as we discuss in the following. In the close vicinity of all defects, the observed deflections and trajectories of beams also agree with numerical predictions of the two mutually consistent models (Fig. 1).

Steering, localization and fission of beams

Photo-patterned arrays of vortices (Fig. 3a,b,i,j, Extended Data Fig. 6 and Supplementary Videos 3 and 4) allow for even more striking control of light propagation, including light confinement within regions comparable to the unit cell (Figs. 3 and 4, Extended Data Figs. 7 and 8 and Supplementary Videos 5 and 6), where winding numbers of defects add to zero within their repeat units. For example, $k = 3$ vortices, revealed by twelve alternating bright and dark brushes in polarizing optical micrographs with a corresponding 6π azimuthal $\mathbf{n}(\mathbf{r})$ rotation around them (Fig. 3a–c), are compensated by multiple $k = -1$ and $k = -1/2$ vortices accompanied by four and two, respectively, dark or bright brushes. Interestingly, bright-field micrographs reveal that the core of each $k = 3$ defect locally splits into six half-integer vortices arranged into a hexagon (Fig. 3b). This is driven by minimization of the free energy of vortices, which scales proportionally to k^2 and tends to replace one $k = 3$ defect with six $k = 1/2$ counterparts. Details of the local splitting under the conditions of the $k = 3$ defect being enforced at confining surfaces are revealed by Landau–de Gennes free-energy-based numerical simulations (Fig. 3d), showing the geometries of $\mathbf{n}(\mathbf{r})$ and a reduced scalar order parameter. While the boundary conditions fix the $k = 3$ structure at confining glass plates, the defect splits into six bulging-out $k = 1/2$ singular-core vortices in the cell's midplane.

To probe interactions of light with vortex arrays, we fix the incident beam's position to pass through the sample's midplane while laterally translating the cell so that the soliton is launched at different locations at the cell's edge (Methods, Fig. 2b and Supplementary Videos 5 and 6). Overlaying the soliton trajectories with polarizing optical micrographs in both experiments and computer simulations vividly reveals the key principles of the light steering. Depending on the beam entry point relative to the array, beam deflections due to individual vortices accumulate to allow for beam meandering, bending backward and even localization (Fig. 3e–h), again in a striking agreement between experiments and modelling. Analysis of the light interaction with the hexagonally split half-integer cores of $k = 3$ vortices allows for qualitatively describing them as 'topological gates' capable of sending beams along different trajectories (Supplementary Video 5), depending on the soliton's propagation relative to the six singular cores. Each $k = 3$ topological gate is capable of 90° bending of the light beam, with the geometry of the square-periodic lattice of $k = 3$ defects allowing for the sending of the beam between the vortices (Fig. 3a,c,e,f). Beam injections at different positions controlled by fine sample translations yield assorted ray trajectories, as depicted with the different colours overlaid for the same vortex array in Fig. 3g,h.

Arrays of $k = 1$, $\Psi_0 = 0$ defects arranged into quasi-hexagonal repeat units, with cores split into two $k = 1/2$ vortex lines (Fig. 3i–l)

https://doi.org/10.1038/s41563-022-01414-y

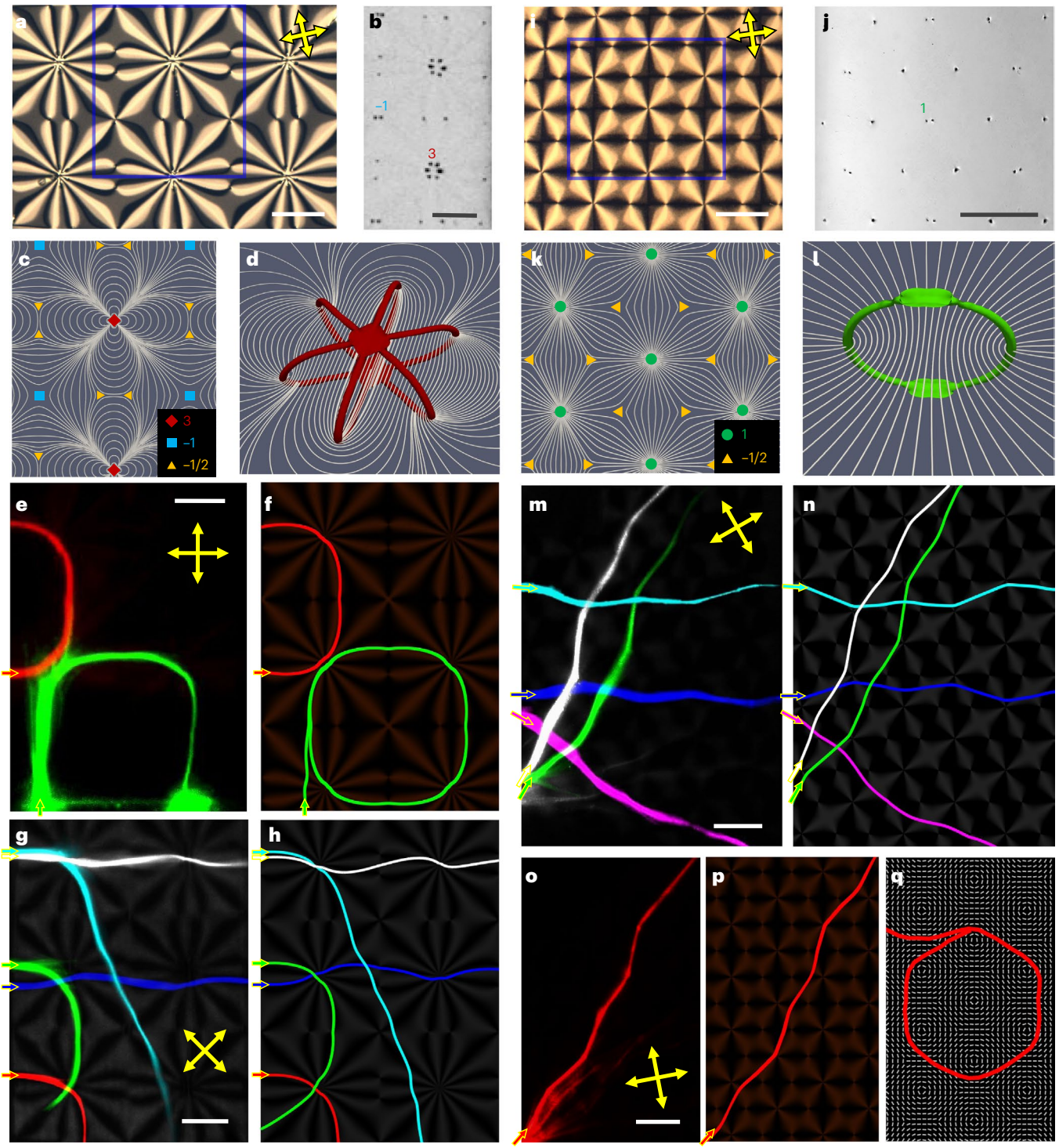

Fig. 3 | Interactions of optical solitons with arrays of vortices. a, Polarizing optical micrograph of an array containing $k = 3$, $k = -1$ and $k = -1/2$ vortices. **b**, The bright-field optical micrograph showing dark dots that correspond to the singular/melted cores of half-integer vortices, depicting how the $k = 3$ and $k = -1$ cores split into six and two half-integer defects in the cell midplane, respectively. **c**, The corresponding $\mathbf{n}(\mathbf{r})$ (white streamlines) within the blue boxed region in **a**; different vortex locations are marked by filled red diamonds, blue squares and orange triangles. **d**, Computer-simulated splitting of the $k = 3$ defect core into a hexagon of half-integer vortices, with the red isosurfaces showing regions of a reduced scalar order parameter of 0.43 and lower. **e**, Beam trajectories with accumulating light deflections bending them backward (red) or into closed loops (green). **f**, The computer-simulated analogues obtained with the Hamiltonian approach, overlaid on top of corresponding polarizing optical micrographs. **g**,**h**, Distinct vortex-guided experimental (**g**) and computer-simulated (**h**) ray trajectories distinguished by false colours. **i**–**k**, An array with $k = 1$ vortices shown as in **a**–**c**, respectively, with experimental micrographs and a simulation of $\mathbf{n}(\mathbf{r})$ and defects. The bright-field micrograph (**j**) shows local splitting of $k = 1$ vortex cores into two half-integer defects. **l**, Simulated splitting of the $k = 1$ vortex core showing $\mathbf{n}(\mathbf{r})$ and regions of a reduced scalar order parameter of 0.5 and lower (green). **m**–**p**, Various experimental (**m**,**o**) and simulated (**n**,**p**) beam trajectories guided by an array of $k = 1$ vortices. **q**, Closed-loop light trajectory formation for this array in a LC with optical anisotropy of 0.365. Double yellow arrows mark orientations of crossed polarizers. All scale bars are 200 μm. Arrows with yellow frame mark the entry positions and directions of light beams in **e**–**h**, **m**–**p**.

https://doi.org/10.1038/s41563-022-01414-y

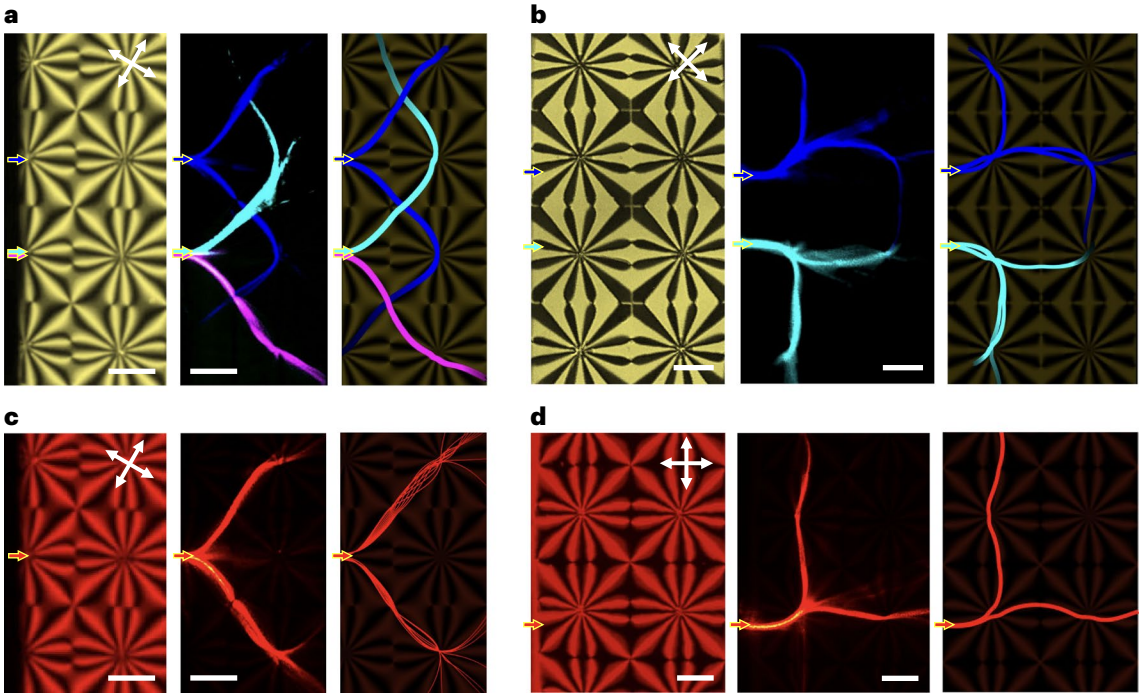

Fig. 4 | Vortex-mediated fission of optical solitons. a–d, Interaction of light beams with arrays containing $k = 3$, $\Psi_0 = \pi/2$ vortices (**a** and **c**) and $k = 3$, $\Psi_0 = 0$ vortices (**b** and **d**). The left image in each panel shows polarizing optical micrographs, the middle shows experimental beam trajectories and the right shows the superimposed computer-simulated light trajectories and polarizing micrographs. In **a** and **b**, optical trajectories of the solitons are distinguished by false colours before and after fission events, for clarity. The arrows with a yellow frame show the optical soliton launching sites. Double white arrows mark the orientations of crossed polarizers. All scale bars are 200 µm, showing different dimensions of the studied defect arrays.

and compensated by $k = -1/2$ vortices, also cause beam meandering and deflection (Fig. 3m–q). Different from the $k = 3$ defects, however, light localization can occur only at large values of optical anisotropy of ~0.36 (Methods and Fig. 3q), which is accessible in LCs. Optical solitons traverse the sample with distinct light-steering vortices in a manner consistent with model predictions (Fig. 3m–p). Despite the common existence of many possible paths for a beam of finite width (Supplementary Video 6), we also observe single solitonic trajectories (Fig. 3o). Such interactions generate different soliton morphologies, including lightning-like and zigzag-like trajectories. Even slight changes of the entry locations of the optical solitons yield a dramatic, fascinating evolution of light steering by this vortex array (Supplementary Videos 5 and 6).

The scalar orientational order parameter is reduced within the cores of vortices at ~10 nm scales, much smaller than the diameter of the solitonic beams with which they interact. Such vortices can mediate the fission of solitonic light when it passes through the defect's core and its constituent parts deflect in opposite directions after an emergent interaction that splits the incident beam (Fig. 4, Extended Data Fig. 8 and Supplementary Video 5). The power of the incident laser beam can be tuned to maintain the solitonic nature of the traversing light, thus enabling fission of the original soliton into two or more daughter solitons. For example, a square array of $k = 3$ vortices, shown in Fig. 4a, photo-patterned at the cell's edge to align the incident beams with the vortex lines, causes various fascinating soliton fission events when the beam passes through the hexagonally split cores of vortices. The soliton launching positions, labelled by arrows in the left images of Fig. 4, determine this behaviour: slight shifts of the beam away from the defect core result in one or both daughter beams losing their solitonic nature and decaying due to scattering, so that most commonly a single vortex–soliton interaction trajectory is observed instead of the fission phenomenon (Extended Data Fig. 8). Key to this behaviour is that solitons pass through cores of vortices (Fig. 4a,c and Supplementary Video 4), which at high powers can yield sequential fissions at different vortex sites. Numerical modelling fully reproduces the behaviour of both parent and daughter solitons by tracing multiple rays within the finite-width solitons (Fig. 4). Our experiments reveal how this fission behaviour depends on the smoothness (resolution) of surface photo-patterning, lattice parameters and the symmetry of defect arrays (Fig. 4 and Extended Data Fig. 8), and can be controlled by manipulating the split-core defects with laser tweezers (Supplementary Video 7).

Control of light steering by external stimuli

The intrinsic stimuli-responsive nature of LCs allows for tuning the studied vortex-mediated light-steering behaviour. Electric fields reconfigure the defect morphology in a facile manner (Fig. 5a–d and Extended Data Fig. 9) through coupling to $\mathbf{n}(\mathbf{r})$ (ref. [36]). Due to our LC's positive dielectric anisotropy, the electric field tends to align the initially in-plane $\mathbf{n}(\mathbf{r})$ to point along the cell normal while stretching and reconnecting the vortices (Fig. 5d and Extended Data Fig. 9a). In turn, the reconfigured $\mathbf{n}(\mathbf{r})$ and vortices interact with light in dramatically different ways, as shown quantitatively for selected entry positions marked in Fig. 5a (y_1, y_2 and y_3). For example, an optical soliton launched from position y_2 experiences a monotonous change of the steering angle from about −180° to −10° with increasing voltage to 5.0 V, whereas solitons launched at y_1 and y_3 change even the deflection directions within this voltage range (Fig. 5a–d and Extended Data Fig. 9b,d). Patterned indium tin oxide electrodes can customize this control even further, depending on the need (Extended Data Fig. 9); for example, the topological array regions near cell edges can be left non-responsive to the electric field by etching the corresponding parts of the electrode. The steering behaviour directly correlates with the manipulation of the spatial positions of vortex lines driven by electric fields (Extended Data Fig. 9).

https://doi.org/10.1038/s41563-022-01414-y

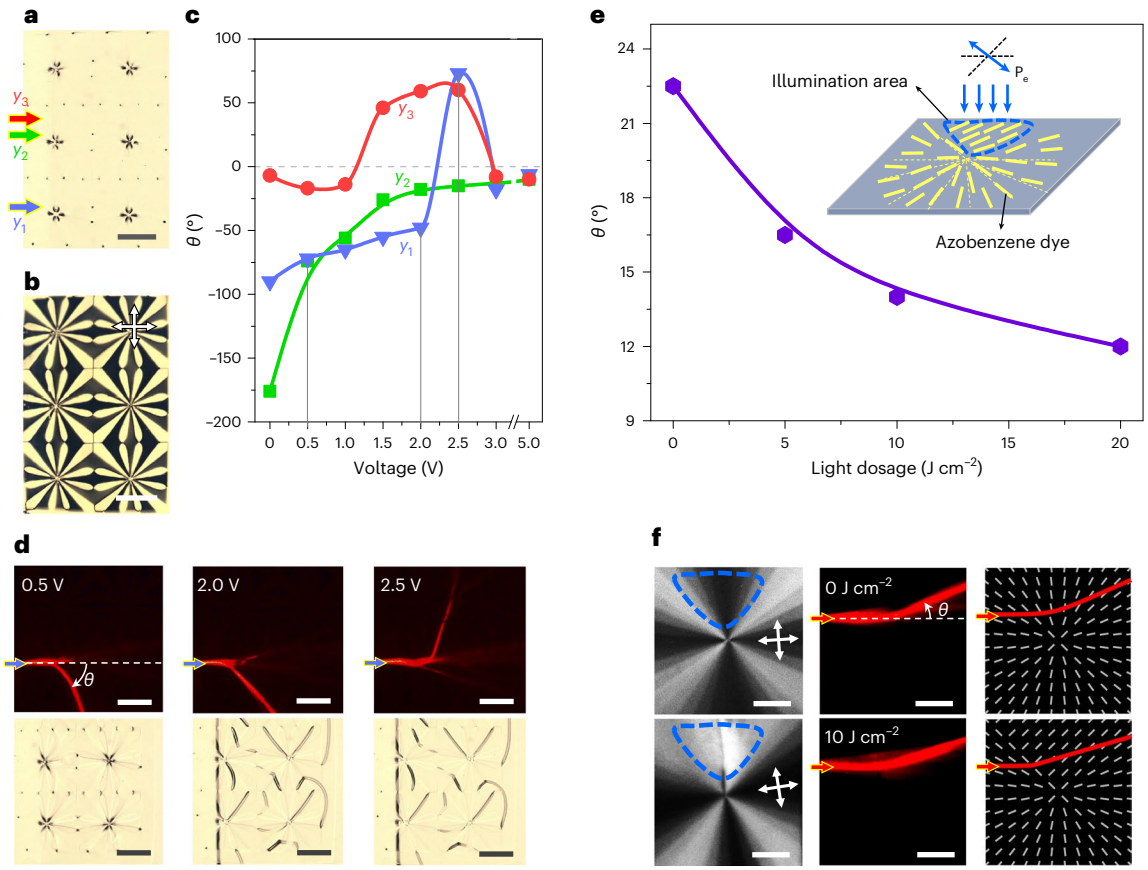

Fig. 5 | Electrical and optical control of light deflection. a–**c**, Voltage dependence of an accumulated light deflection angle θ, which is defined in **d**, inside a vortex array photographed without (**a**) and with (**b**) crossed polarizers. Voltage dependencies of θ for beams launched from locations marked in **a** by y_1, y_2 and y_3 are shown by correspondingly coloured solid lines and filled triangles, squares and circles, respectively. **d**, Representative beam trajectories (upper) and bright-field optical micrographs (lower) at 0.5 V, 2.0 V and 2.5 V for an optical soliton launched from y_1 (blue arrow with yellow frame), with corresponding data points marked in **c** using vertical grey lines. **e**, Deflection angle θ versus light dosage imposed on a predefined area marked with a blue dashed line in the inset, within which the local illumination causes realignment of **n**(**r**). Inset is a schematic of **n**(**r**) around a $k = 1$, $\Psi_0 = 0$ vortex post-modified by the linearly polarized blue-light illumination (blue vertical arrows; polarized along the double blue arrow marked by P_e). **f**, Corresponding polarizing micrographs (left) with the illumination area marked in blue dashed closed loops, beam trajectories (middle) and computer-simulated **n**(**r**) and beam trajectories (right) for light dosages of 0 J cm^{-2} (upper) and 10 J cm^{-2} (lower). Double white arrows mark orientations of crossed polarizers. The solid lines in **c** and **e** are guides for the eye only. All scale bars are 200 μm. Arrows with yellow frame mark the entry positions of light beams in **d** and **f**.

Light itself can be used for reconfiguring LC vortices and **n**(**r**) within the topological arrays, providing the advantage of non-contact control[37]. For example, in some samples (Methods), linearly polarized blue-light illumination (inset of Fig. 5e) can be used to realign the photo-patterning azobenzene dye layer, allowing us to reconfigure and post-modify **n**(**r**) and the defects. When a light flux is imposed on a localized area to locally rotate **n**(**r**) by up to 45°, soliton deflection by the vortex changes from the initial 23° to 12° as the illumination dosage increases to 20 J cm^{-2} (Fig. 5e). This all-optical reconfiguration of **n**(**r**) around the vortex is confirmed by polarizing optical micrographs, with experimental changes of the deflection angle reproduced by modelling (Fig. 5f).

Cosmic string analogy and predesigned beam steering

Described by the first homotopy group, LC vortices and cosmic strings have more in common than just the topological identity. For example, the formation of these topological defects at the order–disorder transitions are described by the Kibble–Zurek mechanism for both LCs and the Early Universe Cosmology[5–8]. Dynamics of vortices upon quenching LC materials through a transition from the isotropic to the nematic phase, a material analogue of the Big Bang, were used to model the analogous behaviour of cosmic strings[9,10] well before recent attempts to study them in gravitational wave experiments[11,12]. Predicted by Einstein, the discovery that rays of light passing by massive extraterrestrial objects can be bent by the warped spacetime through which they travel continues to fascinate researchers and the public alike[29], and the elusive cosmic strings are also expected to steer light[13–20,29–32]. This steering arises from the cone-shaped spacetime of cosmic strings, which stems from the connecting edges of the flat spacetime, separated at a given deficit angle $\Delta\phi$ (Fig. 6a,b)[30–32], a construction known as the 'Volterra's process' that is also used in studies of LC defects[33]. Light-steering properties of straight cosmic strings and linear fragments of LC vortices can both be described analytically by effective metrics (Methods and Fig. 6c,d)[34], which are similar in the weak lensing regime for the simplest LC and cosmological defects[14,30,35]. The light-guiding power of cosmic strings is determined by a parameter $4G\mu/c^2$, with G being the gravitational constant, μ, the linear mass density of the cosmic string and c, the speed of light in vacuum. An analogous parameter describing the steering of the extraordinary mode of light by LC vortices is $\Delta n/n_e$. Predicted LC-defect-mediated light deflection angles θ can be comparable to or by far exceed their counterparts measured for the

https://doi.org/10.1038/s41563-022-01414-y

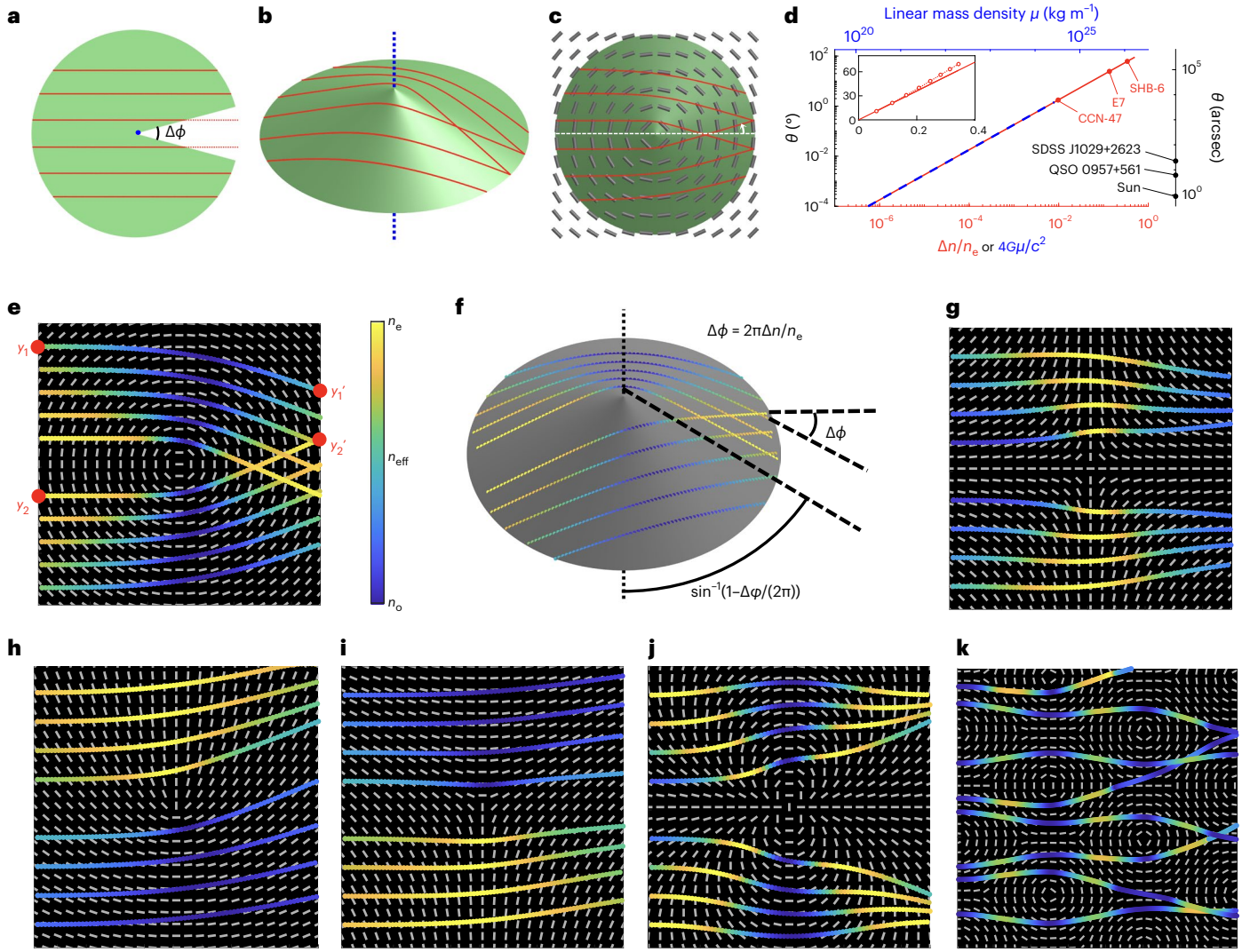

Fig. 6 | Cosmology analogy, light deflection by LC vortices and effective geometry. a–**c**, Schematics of a conical spacetime (green), which emerges from connecting edges of a flat spacetime (**a**) separated by the deficit angle $\Delta\phi$. The light trajectories (red lines) are distorted due to either a cosmic string (blue dashed line) or the LC vortex with concentric $\mathbf{n}(\mathbf{r})$ configuration, shown by grey cylinders in **c**. The $\Delta\phi$ is marked in **a**, and the light deflection angle θ is marked with a white arrow in **c**. **d**, The θ of light rays passing near a cosmic string (blue) or a $k = 1$, $\Psi_0 = \pi/2$ LC vortex line (red). Red dots correspond to LCs CCN-47 ($\Delta n = 0.015$), E7 ($\Delta n = 0.24$) and SHB-6 ($\Delta n = 0.79$)[41–43]. The inset with a linear scale shows the values obtained from a Hamiltonian-based simulation (open circles, with dashed line serving as a guide to the eye) and from theoretical prediction (solid line; Methods). On the right, examples of known gravitational deflections by extraterrestrial objects are shown on the same scale as θ on the left, on top of an added scale of the arcsec units used in cosmology. **e**, Spatial variation of an effective refractive index (n_{eff}) seen by light traversing around the $k = 1$, $\Psi_0 = \pi/2$ vortex, presented with a colour scale shown at the right. **f**, The corresponding effective geometry mimicking that of the conic spacetime around a cosmic string. **g**–**k**, Spatial variations of an effective refractive index seen by light traversing around vortices with different winding numbers of $k = -1$ (**g**), $k = 1/2$ (**h**), $k = -1/2$ (**i**) and $k = 2$ (**j**) and an array with $k = 1$ and $k = -1/2$ defects (**k**).

Sun, Twin Quasar QSO 0957+561, the largest separation lensed Quasar SDSS J1029+2623 and other extraterrestrial objects with the strongest known light guiding (Fig. 6d)[38–40]. Depending on Δn, which for known LCs varies from negative values to $\Delta n \approx 0$ and to $\Delta n \approx 0.8$ (refs. [41–43]), one often needs to resort to numerical analysis of the deflection angles (Fig. 6d and Methods)[44–46]. Similar to experimental findings for LC vortices (Extended Data Fig. 4), deflection angles are expected to increase with the topological charge of cosmic strings[47]. However, high-charge defects in both LCs and cosmology lack stability because their energies increase with charge and drive splitting into elementary defects, where this tendency[7] of high-charge photo-patterned LC vortices leads to splitting of their cores (Fig. 3a,b).

Building on the above analogy, topological steering can be explained from the Fermat principle viewpoint, where light selects the shortest optical paths between points like y_1 and y_1' or y_2 and y_2' in Fig. 6e (corresponding to the shortest time needed to travel between these points), so that finding its trajectory is an optimization problem addressed with an effective geometry, analogously to the problem of conic spacetime of cosmic strings, though defined in terms of LC properties (Fig. 6a–d,f). However, the extraordinary mode of light traversing the LC sees a spatially varying effective refractive index (Fig. 6e and Methods), so that beam deflections at each point along its propagation stem from Snell's law applied at imaginary interfaces slicing the medium into thin slabs of constant index[48,49]. Optical axis rotations around vortices are quantized in integers of π, yielding strong light-guiding effects described with transformation optics, analogous to how cosmic strings warp the spacetime to deflect light[2,50], with quantitative insights useful for designing devices (Fig. 6e–k). For example, the net far-field angular deflection of a beam interacting with a $k = 1$, $\Psi_0 = \pi/2$ vortex (Fig. 6e,f) is $\theta = \Delta\phi/2 = \pi\Delta n/n_e$, yielding

the range $\theta = 21.7–24°$, depending on the wavelength for which the Δn and n_e values are used. This matches the θ experimentally measured at distances much larger than the shortest vortex-beam distance, providing insights into how desired steering effects can be achieved by choosing specific materials and tuning the effective LC birefringence with external stimuli like electric fields.

While we focused on light propagation in a plane orthogonal to the vortices, with the optical axis patterns also bound to this plane, our findings can be extended to more complex patterns of vortices, exceeding the insights related to analogies with cosmic strings. For example, in three dimensions the $\pi_1(\mathbb{S}^2/\mathbb{Z}_2) = \mathbb{Z}_2$ LC vortices allow for confining twisted regions, with a refractive index seen by the extraordinary light higher than that of the surrounding medium (Extended Data Fig. 10), so that topological steering can also arise from waveguiding due to total internal reflections (here π_1 refers to the first homotopy group, $\mathbb{S}^2$ refers to two spheres and $\mathbb{Z}_2$ is the cyclic group of order 2). By using such patterns of LC vortex lines, highly complex light-steering trajectories can be designed, such as trefoil knots (Extended Data Fig. 10), albeit three-dimensional patterning of LC vortices will need to be advanced further to exploit such effects for technological applications.

Conclusions and outlook

We have demonstrated how LC vortices can continuously bend beams of light, with the strong light-steering effects in large-Δn materials of interest for myriads of technological applications. To enhance Δn, LCs can be doped with nanoparticles[37,51,52], including MoS_2 with $\Delta n \approx 3.0$ (ref. [53]) or, alternatively, metamaterials with giant Δn values; and analogues of vortices can be fabricated[54,55]. In the simplest cases, LC vortex–light interactions mimic the interaction of light with cosmic strings. Multi-defect patterns enhance the light-steering effects in a controlled way, which potentially could be extended further to dynamic vortices undergoing reconnections and closed-loop generations. Although solitonic light was used in our experiments, topological steering can be achieved for non-solitonic beams by suppressing scattering through polymerization or by miniaturizing samples to minimize intensity loss within slowly varying patterns of the optical axis. This cosmology-inspired topological steering may find applications in electrically and optically reconfigurable multiplexing and steering devices, logic gates, telecommunications, cloaking, singular optics, virtual reality designs and so on, expanding the technological utility of topological defects and solitons in LCs.

Online content

Any methods, additional references, Nature Portfolio reporting summaries, source data, extended data, supplementary information, acknowledgements, peer review information; details of author contributions and competing interests; and statements of data and code availability are available at https://doi.org/10.1038/s41563-022-01414-y.

References

1. Khoo, I. C. & Wu, S.-T., *Optics and Nonlinear Optics of Liquid Crystals* (World Scientific, 1993).
2. Wu, J. S. & Smalyukh, I. I. Hopfions, heliknotons, skyrmions, torons and both abelian and nonabelian vortices in chiral liquid crystals. *Liq. Cryst. Rev*. https://doi.org/10.1080/21680396.2022.2040058 (2022).
3. Tabiryan, N. V. et al. Advances in transparent planar optics: enabling large aperture, ultrathin lenses. *Adv. Opt. Mater.* **9**, 2001692 (2021).
4. Lavrentovich, O. D., Shiyanovskii, S. V. & Voloschenko, D. Fast beam steering cholesteric diffractive devices. *Proc. SPIE* **3787**, 149–155 (1999).
5. Kibble, T. Topology of cosmic domains and strings. *J. Phys. A* **9**, 1387–1398 (1976).
6. Zurek, W. H. Cosmological experiments in superfluid helium? *Nature* **317**, 505–508 (1985).
7. Chaikin, P. M. & Lubensky, T. C. *Principles of Condensed Matter Physics* (Cambridge Univ. Press, 1995).
8. Smalyukh, I. I. Knots and other new topological effects in liquid crystals and colloids. *Rep. Prog. Phys.* **83**, 106601 (2020).
9. Chuang, I., Durrer, R., Turok, N. & Yurke, B. Cosmology in the laboratory: defect dynamics in liquid crystals. *Science* **251**, 1336–1342 (1991).
10. Bowick, M. J., Chandar, L., Schiff, E. A. & Srivastava, A. M. The cosmological Kibble mechanism in the laboratory: string formation in liquid crystals. *Science* **263**, 943–945 (1994).
11. Blasi, S., Brdar, V. & Schmitz, K. Has NANOGrav found first evidence for cosmic strings? *Phys. Rev. Lett.* **126**, 041305 (2021).
12. Ellis, J. & Lewicki, M. Cosmic string interpretation of NANOGrav pulsar timing data. *Phys. Rev. Lett.* **126**, 041304 (2021).
13. Mukai, H., Fernandes, P. R. G., de Oliveira, B. F. & Dias, G. S. Defect-antidefect correlations in a lyotropic liquid crystal from a cosmological point of view. *Phys. Rev. E* **75**, 061704 (2007).
14. Satiro, C. & Moraes, F. A liquid crystal analogue of the cosmic string. *Mod. Phys. Lett. A* **20**, 2561–2565 (2005).
15. Satiro, C. & Moraes, F. On the deflection of light by topological defects in nematic liquid crystals. *Eur. Phys. J. E* **25**, 425–429 (2008).
16. Simões, M. & Pazetti, M. Liquid-crystals cosmology. *Eur. Phys. Lett.* **92**, 14001 (2010).
17. Pereira, E. & Moraes, F. Diffraction of light by topological defects in liquid crystals. *Liq. Cryst.* **38**, 295–302 (2011).
18. de M. Carvalho, A. M., Satiro, C. & Moraes, F. Aharonov-Bohm–like effect for light propagating in nematics with disclinations. *Europhys. Lett.* **80**, 46002 (2007).
19. Vilenkin, A. Cosmic strings as gravitational lenses. *Astrophys. J.* **282**, L51–L53 (1984).
20. Fischer, U. R. & Visser, M. Riemannian geometry of irrotational vortex acoustics. *Phys. Rev. Lett.* **88**, 110201 (2002).
21. Martinez, A., Mireles, H. C. & Smalyukh, I. I. Large-area optoelastic manipulation of colloidal particles in liquid crystals using photoresponsive molecular surface monolayers. *Proc. Natl Acad. Sci. USA* **108**, 20891–20896 (2011).
22. Peng, C., Turiv, T., Guo, Y., Wei, Q. H. & Lavrentovich, O. D. Command of active matter by topological defects and patterns. *Science* **354**, 882–885 (2016).
23. Wang, M., Li, Y. & Yokoyama, H. Artificial web of disclination lines in nematic liquid crystals. *Nat. Commun.* **8**, 388 (2017).
24. Born, M. & Wolf, E. *Principles of Optics* (Cambridge Univ. Press, 1999).
25. Peccianti, M. & Assanto, G. Nematicons. *Phys. Rep.* **516**, 147–208 (2012).
26. Peccianti, M., Conti, C., Assanto, G., De Luca, A. & Umeton, C. Routing of anisotropic spatial solitons and modulational instability in liquid crystals. *Nature* **432**, 733–737 (2004).
27. Kivshar, Y. S. & Agrawal, G. P. *Optical Solitons: from Fibers to Photonic Crystals* (Academic Press, 2003).
28. Poy, G. et al. Interaction and co-assembly of optical and topological solitons. *Nat. Photon.* **16**, 454–461 (2022).
29. Rindler, W. *Relativity: Special, General, and Cosmological* (Oxford Univ. Press, 2001).
30. Vilenkin, A. Gravitational field of vacuum domain walls and strings. *Phy. Rev. D* **23**, 852–857 (1981).
31. Copeland, E. J. & Kibble, T. W. B. Cosmic strings and superstrings. *Proc. R. Soc. A* **466**, 623–657 (2010).
32. Sazhin, M. V. et al. Gravitational lensing by cosmic strings: what we learn from the CSL-1 case. *Mon. Not. R. Astron. Soc.* **376**, 1731–1739 (2007).

33. Kleman, M. & Lavrentovich, O. D. *Soft Matter Physics: An Introduction* (Springer New York, 2003).
34. Sátiro, C. & Moraes, F. Lensing effects in a nematic liquid crystal with topological defects. *Eur. Phys. J. E* **20**, 173–178 (2006).
35. Figueiredo, D., Moraes, F., Fumeron, S. & Berche, B. Cosmology in the laboratory: an analogy between hyperbolic metamaterials and the Milne universe. *Phy. Rev. D* **96**, 105012 (2017).
36. Yeh, P. & Gu, C. *Optics of Liquid Crystal Displays* (John Wiley & Sons, 1999).
37. Liu, Q. et al. Plasmonic complex fluids of nematiclike and helicoidal self-assemblies of gold nanorods with a negative order parameter. *Phys. Rev. Lett.* **109**, 088301 (2012).
38. Lebach, D. E. et al. Measurement of the solar gravitational deflection of radio waves using very-long-baseline interferometry. *Phys. Rev. Lett.* **75**, 1439–1442 (1995).
39. Chang, K. & Refsdal, S. Flux variations of QSO 0957+561A,B and image splitting by stars near the light path. *Nature* **282**, 561–564 (1979).
40. Inada, N. et al. SDSS J1029+2623: a gravitationally lensed quasar with an image separation of 22."5. *Astrophys. J.* **653**, L97 (2006).
41. Dhara, S. & Madhusudana, N. V. Physical characterisation of 4′-butyl-4-heptyl-bicyclohexyl-4-carbonitrile. *Phase Transit.* **81**, 561–569 (2008).
42. Li, J., Wu, S.-T., Brugioni, S., Meucci, R. & Faetti, S. Infrared refractive indices of liquid crystals. *J. Appl. Phys.* **97**, 073501 (2005).
43. Gauza, S., Wen, C. H., Wu, S.-T., Janarthanan, N. & Hsu, C. S. Super high birefringence isothiocyanato biphenyl-bistolane liquid crystals. *Jpn. J. Appl. Phys.* **43**, 7634 (2004).
44. Cohen, A. G. & Kaplan, D. B. The exact metric about global cosmic strings. *Phys. Lett. B* **215**, 67–72 (1988).
45. Zhang, Y. L., Dong, X. Z., Zheng, M. L., Zhao, Z. S. & Duan, X. M. Steering electromagnetic beams with conical curvature singularities. *Opt. Lett.* **40**, 4783–4786 (2015).
46. Barros, W., Santos, A. D. P. & Pereira, E. Concentrating, diverging, shifting, and splitting electromagnetic beams using a single conical structure. *J. Appl. Phys.* **128**, 093105 (2020).
47. Comtet, A. & Gibbons, G. W. Bogomol'nyi bounds for cosmic strings. *Nucl. Phys. B* **299**, 719–733 (1988).
48. Poy, G., Hess, A. J., Smalyukh, I. I. & Slobodan Žumer, S. Chirality-enhanced periodic self-focusing of light in soft birefringent media. *Phys. Rev. Lett.* **125**, 077801 (2020).
49. Hess, A., Poy, G., Tai, J.-S. B., Zumer, S. & Smalyukh, I. I. Control of light by topological solitons in birefringent media. *Phys. Rev. X* **10**, 031042 (2020).
50. Satiro, C., de, M., Carvalho, A. M. & Moraes, F. An asymmetric family of cosmic strings. *Mod. Phys. Lett. A* **24**, 1437–1442 (2009).
51. Arakawa, Y. et al. Design of an extremely high birefringence nematic liquid crystal based on a dinaphthyl-diacetylene mesogen. *J. Mater. Chem.* **22**, 13908–13910 (2012).
52. Liu, Q., Campbell, M. G., Evans, J. S. & Smalyukh, I. I. Orientationally ordered colloidal co-dispersions of gold nanorods and cellulose nanocrystals. *Adv. Mater.* **26**, 7178–7184 (2014).
53. Ermolaev, G. A. et al. Giant optical anisotropy in transition metal dichalcogenides for next-generation photonics. *Nat. Commun.* **12**, 854 (2021).
54. Kats, M. A. et al. Giant birefringence in optical antenna arrays with widely tailorable optical anisotropy. *Proc. Natl Acad. Sci. USA* **109**, 12364–12368 (2012).
55. Sheng, C., Chen, H. & Zhu, S. Definite photon deflections of topological defects in metasurfaces and symmetry-breaking phase transitions with material loss. *Nat. Commun.* **9**, 4271 (2018).

Methods

Sample preparation

To fabricate LC cells, glass plates with or without transparent electrodes were spin-coated using 1.0 wt% azobenzene dye SD1 in dimethylformamide at 3,000 r.p.m. for 45 s and subsequently baked on a hotplate at 100 °C for 10 min to evaporate the residual solvent. Glass substrates with indium tin oxide coatings were used to fabricate cells for experiments involving application of electric fields[56–59]. To define the gap between the two confining glass plates, a fast-setting epoxy glue containing silica spacer spheres (15–60 μm in diameter, from Thermo Fisher) was placed near the corners of one glass plate (Fig. 2b and Extended Data Fig. 1a); the other glass plate was then lapped atop, leaving a small fraction of the electrode layer exposed for the connection to an external voltage supply (GFG-8216A, GW Instek). After the epoxy was fully solidified, a coverslip with a thickness of 0.17 mm was glued to the cell edge (Fig. 2b and Supplementary Notes), as needed for focusing a laser beam at the cell entry to launch a nematicon. The surface of the coverslip was pretreated with a polyvinyl alcohol (Dupont) film and mechanically rubbed using velvet cloth to impose strong and uniform boundary conditions[60]. The cell was then photo-patterned with a predesigned geometry for $\mathbf{n}(\mathbf{r})$ to induce the desired vortices via the method described in the following. After the photo-patterning, a commercial LC mixture E7 (Shijiazhuang Chengzhi Yonghua Display Material Co.) was filled into the empty cell by capillary forces at an elevated temperature of 100 °C and then quenched to room temperature under ambient conditions.

Photo-patterning of vortices

Our mesostructured LC vortices were architected by spatially orienting LC molecules on the inner surfaces of the two confining glass plates with an ~10-nm-thin layer of the azobenzene dye[61], a polarization-responsive photoalignment material. Upon being illuminated with a small dose (that is, ~200 mJ cm^{-2}) of linearly polarized blue light, the azobenzene moieties of the dye molecules orient orthogonally to the light's polarization direction, yielding robust surface boundary conditions[61] for the $\mathbf{n}(\mathbf{r})$ of the LC (Extended Data Fig. 1a). By using a LC microdisplay, all desired two-dimensional boundary condition geometries for $\mathbf{n}(\mathbf{r})$ can be predefined through spatially illuminating linearly polarized blue-light patterns, as controlled on a pixel-by-pixel basis with computer software. As schematically shown in Extended Data Fig. 1b, a blue-light pattern generated by computer is projected through the microdisplay with 1,024 × 768 pixels (EMP-730, Epson) and then relayed by three lenses to the back aperture of an objective. The blue light imprinting the pattern is focused on the azobenzene dye layers. The two azobenzene dye layers on the opposite inner surfaces of the confining glass plates can be patterned for boundary conditions sequentially or at the same time, depending on the cell gap relative to the focus depth of the objective[62]. In this study, we did simultaneous patterning of the two surfaces of the cells by using low-magnification ×4 objectives (numerical aperture of 0.13) and relatively small cell gaps. The desired linear polarization is controlled by a half-wave plate and a linear polarizer inserted at appropriate locations along the optical path (Extended Data Fig. 1b). By means of multi-step illuminations synchronized with the linear polarization rotation, an arbitrary predesigned structure of boundary conditions can be generated.

For the needs of patterning LC vortices and their arrays, as schematically illustrated in Extended Data Fig. 1c, the entire structure was separated into angular segments of roughly constant in-plane director orientation. The $\mathbf{n}(\mathbf{r})$ boundary condition for each pattern of the same angular segment was generated by the same linearly polarized excitation light projected onto the sample. After multiple sequential projections done for different azimuthal orientations of $\mathbf{n}(\mathbf{r})$, a complete geometry of two-dimensional vortices was imprinted into the spatially oriented azobenzene dye layer. The angular resolution of patterning, defined by discrete changes of the linear polarization direction between two adjacent segments, was controlled to be within 1° to 45°, depending on the need. Lateral dimensions of the light-programmed $\mathbf{n}(\mathbf{r})$ structures can be varied from micrometres to millimetres, as defined by the projected size of the blue-light pattern and the magnification of an objective (if any).

Optical imaging, video microscopy and laser tweezers

A charge-coupled device camera (Grasshopper3, from PointGrey) mounted on an upright BX-51 or inverted IX-71 microscope (both from Olympus) was used for optical video microscopy. Olympus objectives with ×2, ×4 and ×10 magnifications and numerical apertures of 0.06–0.4 were used for bright-field optical imaging. The microscopes were additionally equipped with pairs of insertable and rotatable linear polarizers and both quarter-wave and half-wave plates for the polarizing optical microscopy experiments. Images of solitonic light trajectories, based on out-of-plane scattering of laser light, were generated starting from different entry positions relative to the LC vortices and then superimposed (examples in Figs. 1, 3 and 4) by using the image-processing software ImageJ (freeware obtained from the National Institutes of Health). Also, the microscopic videos were combined with the same software (Supplementary Videos 1, 2 and 4–6).

The laser tweezers set-up, which we used to manipulate the defects, is based on an ytterbium-doped fibre laser (YLR-10-1064, IPG Photonics, operating at 1,064 nm) and a phase-only spatial light modulator (P512-1064, Boulder Nonlinear Systems) with 512 pixels × 512 pixels, each with a size of 15 μm × 15 μm (refs. [63,64]) integrated with an inverted IX-81 optical microscope (Olympus)[65]. The beam from the laser is first reflected off the spatial light modulator and then projected to the back aperture of an objective. The computer-generated holograms are supplied to the spatial light modulator by computer software at a rate of 15 Hz, ensuring real-time manipulation. Bright-field optical images revealing details of laser manipulation are captured and videos are recorded using the same Grasshopper3 charge-coupled device camera. At a nominal laser power of ~1 W, a ×20 objective with a numerical aperture of 0.5 was used to focus the laser beam for locally heating and melting the LC by prompting a transition from the nematic to isotropic phase and then quenching back to the nematic state (Supplementary Video 7).

Excitation of nematicons and observation of their steering

Optical interactions between LC vortices and traversing light beams were observed with an inverted IX-73 microscope (Olympus; Fig. 2), where a white-light source with a corresponding linear polarization state (denoted by P in Fig. 2a) illuminated the back aperture of a condenser whose back-aperture iris was closed to a pinhole for a coherent plane-wave incident upon the sample (Fig. 2b). A red bandpass filter (FF01-640/14-25, Semrock) was placed before the microscope's condenser to block the violet-blue component of the imaging light during the polarizing microscopy observations of the beam behaviour in the LC medium, in order to eliminate unintentional realignment of the azobenzene molecules within the alignment layers by the imaging light. A viewing objective with a magnification of ×4 and numerical aperture of 0.13 was used to capture the out-of-plane light scattering to trace the beam trajectories. The captured light then passed through an analyser (denoted by A in Fig. 2a) before reaching a digital camera (FLIR BFS-U3-51S5C-C), which recorded the interactions between the solitonic light beam and the LC vortices. This FLIR camera has an enhanced sensitivity in the near-infrared spectral range and thus, is suitable for tracing light trajectories based on out-of-plane scattered light from optical solitons generated in both visible and infrared spectral ranges, as described below. To enable fine and robust translations of the LC sample with photo-patterned vortices, a three-dimensional nanopositioning stage was integrated with the microscope[66], further allowing in-sample-plane optical coupling and through-sample-plane beam characterization. There were two sources of light beams used in this work: one originated from a 200 mW, 650 nm diode laser (OXlasers)

and the other was generated by a 500 mW, 1,064 nm diode-pumped solid-state laser (Laserglow). A ×10 coupling objective with a numerical aperture of 0.4 was used to introduce the light beam with its focal point near the edge-attached coverslip (Fig. 2b). The beam's full width for the two lasers used at the entry point inside the LC cell was measured to be between 20 and 40 μm.

Optical solitons were created in the LC to enable long-range propagation of the laser beams at a minimum loss of intensity. An optical soliton in the LC medium (Fig. 2c–e), dubbed a 'nematicon', is a fascinating realization of self-reinforcing wave solutions relying on nonlinear couplings to compensate for the dispersive effects (Fig. 2f–h)[25,48,67,68]. The nonlinearity arising from the reorientation of $\mathbf{n}(\mathbf{r})$ along the electric field of a traversing light beam is associated with the input beam's power P_{in}, that is, the angle $\delta = \delta_0 + \Delta\delta(P_{in})$, where δ_0 (δ) is the initial (final) angle between $\mathbf{n}(\mathbf{r})$ and the linear polarization of the input beam (Fig. 2c–e), and $\Delta\delta(P_{in})$ is the change in $\mathbf{n}(\mathbf{r})$ orientations. When the beam power increases above a threshold value (~10 mW), reorientation of $\mathbf{n}(\mathbf{r})$ emerges and induces a focusing-lens-like refractive index distribution, enabling compensation for the beam's diffraction, and a nematicon is therefore established (Fig. 2c–e). In order to observe how these nematicons are generated and how the nematicon power impacts the interaction with LC vortices, neutral density filters (Thorlabs) were inserted along the optical path, allowing us to facilely tune the beam power near the coverslip from 0 to 80 mW for the 650 nm laser and from 0 to 200 mW for the 1,064 nm laser. The polarization of the beam was fixed to be oriented along the cell edge by using a polarized-beam-splitting cube and a rotatable half-wave plate correlated with the beam wavelength (Supplementary Notes). In our experiments, we have noted that angular deflections of nematicons caused by LC vortices were the same as what was observed for beams of light at powers below the threshold value needed for nematicon generation, albeit these optical solitons could propagate much farther within the LC medium (Supplementary Notes), enabling our study of vortex–light interactions.

Modelling of optical soliton deflections and trajectories

We used two ray-based approaches to model optical trajectories inside birefringent media like the commercial nematic LC mixture E7. In the Lagrangian approach, the model is based on the notion that the path of a lossless, non-scattering ray follows the Fermat principle, stating that, among all possible paths, the light trajectory is the one that takes the least time, minimizing the integral[34]

$$F = \int N_r(s)\,\mathrm{d}s \tag{1}$$

where F is the optical Lagrangian, $N_r(s)$ is the ray index along path s, which is given by ${N_r}^2 = {n_o}^2\cos^2\beta + {n_e}^2\sin^2\beta$ for an extraordinary ray with β being the angle made by the Poynting vector and LC director, and s is the element of arc length along the optical path. For inhomogeneous or birefringent media, N_r depends on the polarization and the direction of light propagation. Equivalently, an optical beam trajectory inside a birefringent material in Euclidean space can be interpreted as a geodesic, or a 'straight' line, inside an effective geometry[69]. In this case, derived from equation (1), the geodesic equation in Riemannian space reads[34,69]

$$\frac{\mathrm{d}^2 r_i}{\mathrm{d}s^2} = -\sum_{i,j} \Gamma^i_{jk}\frac{\mathrm{d}r_j}{\mathrm{d}s}\frac{\mathrm{d}r_k}{\mathrm{d}s}, \tag{2}$$

where r_i, $i = 1, 2, 3$ are the coordinates of a light beam in real space, and Γ^i_{jk} are Christoffel symbols determined by the effective geometry, which is constructed from the ansatz of the LC alignment field $\Psi(y,x) = k\tan^{-1}(y/x) + \Psi_0$ and the optical constants of the nematic mixture E7 (with extraordinary and ordinary refractive indices $n_e = 1.77$ and $n_o = 1.53$, respectively[42]). In polar coordinates, the metric of such LC vortex lines is found to be[34,46]

$$\begin{aligned}\mathrm{d}s^2 &= \left(n_o^2\cos^2\alpha + n_e^2\sin^2\alpha\right)\mathrm{d}r^2 \\ &+ \left(n_o^2\sin^2\alpha + n_e^2\cos^2\alpha\right)r^2\mathrm{d}\phi^2 - \left(n_e^2 - n_o^2\right)\sin(2\alpha)r\mathrm{d}r\mathrm{d}\phi,\end{aligned} \tag{3}$$

with $\alpha = (k-1)\tan^{-1}(y/x) + \Psi_0$. One finds that, after rescaling, a $k = 1$, $\Psi_0 = \pi/2$ vortex line has a metric resembling that of a straight cosmic string with conical spacetime in the weak lensing regime[14,30,31,35,45]:

$$\mathrm{d}s^2 \approx -c^2\mathrm{d}t^2 + \mathrm{d}z^2 + \mathrm{d}r^2 + \left(1 - \frac{4G\mu}{c^2}\right)^2 r^2\mathrm{d}\phi^2, \tag{4}$$

with t being time, $\{z, r, \phi\}$ being the cylindrical coordinate, G being the gravitational constant, μ being the linear mass density of the cosmic string and c being the speed of light in a vacuum. The similarity is evident when the four-dimensional spacetime is projected to a two-dimensional plane described by radius r and azimuth ϕ, assuming other degrees are constant[14]: $\mathrm{d}s^2 = \mathrm{d}r^2 + (1 - 4G\mu/c^2)^2 r^2\mathrm{d}\phi^2$. The deficit angle $\Delta\phi$ of the corresponding space(time) can be found by identifying the total azimuthal angle $2\pi - \Delta\phi = 2\pi(1 - 4G\mu/c^2) = 2\pi(n_o/n_e)$ from the angular term in equations (3) and (4), respectively. Subsequently, the deflection angle θ of a light beam, defined as the total orientational change of the ray until it reaches an observer colinear with the light source and the vortex line (Fig. 6c), is assumed to be half of the deficit angle, the value of which equals the Einstein radius (Fig. 6c,d)[31,32]. Other types of cosmic strings, with other forms of symmetry breaking, may also exist and share similar light-guiding behaviours with different LC vortex lines[50].

The trajectory of energy flow, or an integral curve of the Poynting vector in the classical regime, is then calculated through numerical integration of equation (2) with the fourth-order adaptive Runge–Kutta method. Within our implementation of this method, the initial position and direction of the Poynting vector were chosen to match those in experimental images, like in Fig. 1, and the resulting paths were plotted as green dashed lines (Fig. 1b–f), where only the extraordinary rays were considered.

The second approach, the Hamiltonian method, has been recently used[48,49,70] for light tracing specifically in uniaxial birefringent materials. In short, the Hamiltonian formulation of ray equations was derived from the Fermat principle. To account for the head–tail symmetry of the LC director field around half-integer defects and to make this approach compatible with our tensorial modelling of field configurations, we first rewrote the Hamiltonian of the extraordinary ray in terms of the Q-tensor order parameter:

$$\mathcal{H}^{(e)} = \frac{2\epsilon_\perp + \epsilon_\parallel}{6\epsilon_\perp\epsilon_\parallel}\mathbf{p}^2 + \frac{\epsilon_\parallel - \epsilon_\perp}{3Q_0\epsilon_\perp\epsilon_\parallel}\mathbf{p}^{\mathrm{T}}Q\mathbf{p}, \tag{5}$$

where $\mathbf{p}$ is the wavevector of rays (or the 'momentum' of a virtual propagating point), Q and Q_0 are the tensor and scalar order parameters of the nematic LC, respectively, and $\epsilon_\perp = {n_o}^2$, $\epsilon_\parallel = {n_e}^2$ are the material's ordinary and extraordinary permittivities. The effective refractive index seen by an extraordinary ray (Fig. 6e–k) is given by ${n_{eff}}^2 = \epsilon_\perp\epsilon_\parallel/(\epsilon_\perp\sin^2\gamma + \epsilon_\parallel\cos^2\gamma)$ with γ being the angle between $\mathbf{p}$ and the LC director $\mathbf{n}$. In addition, the effective birefringence for the beam is $\Delta n_{eff} \equiv n_{eff} - n_o = n_o((1 + (\epsilon_\perp/\epsilon_\parallel - 1)\sin^2\gamma)^{-1/2} - 1)$. The governing equations describing the behaviour of rays are then given by the Hamilton equations:

$$\frac{\mathrm{d}\mathbf{r}}{\mathrm{d}s} = \frac{\partial\mathcal{H}^{(e)}}{\partial\mathbf{p}}, \frac{\mathrm{d}\mathbf{p}}{\mathrm{d}s} = -\frac{\partial\mathcal{H}^{(e)}}{\partial\mathbf{r}}, \tag{6}$$

with $\mathbf{r}$ being the position of propagating point. In every numerical iteration, the values of order parameters Q and Q_0 were interpolated

from the given pattern of the LC alignment field, and the light path was calculated by forward Euler integration of equation (6). The light coming from a source at infinity was numerically prepared as parallel rays (Extended Data Fig. 2), and the deflection angle was determined by the total orientational change of d**r** until the ray reaches the observer colinear with the light source and cosmic string (Fig. 6c,d), or for large deflection at a radius from the pattern's centre (Extended Data Fig. 2). In other cases, the starting position and direction of rays were chosen to match those in our experimental images; an exponential decay in intensity of the light beam was artificially introduced for Fig. 4a,b to avoid the overlap of the trajectories and mimic interactions that do not preserve the solitonic nature of the beams upon their splitting. Light trajectories generated with this approach are shown as solid red lines, as an example, in Fig. 1b–f.

To account for the finite width of the optical solitons used in experiments, our modelling of ray trajectories based on the two approaches used multiple rays to numerically reveal effects like optical soliton fission. In this case, an appropriate alignment of the multi-ray numerical counterpart of the finite-width optical soliton relative to the half-integer vortices within the cores of a $k = 3$ vortex not only could reveal the fission itself, but also could reproduce the fine details of daughter soliton propagation and even the secondary fission of daughter solitons (Fig. 4).

In our numerical modelling, a linear optical soliton–vortex interaction is assumed, as in refs. [25,28,48,49]. Even though a nonlinear response of the LC is needed to fully describe the formation of nematicons, ray tracing in the linear optical regime sufficiently reproduces the experimental beam propagation within the LC medium because the light-induced director realignment angles within the solitons are much smaller than the angles corresponding to spatially varying director structures around the studied LC vortices[25,28,48,49].

Landau–de Gennes modelling of LC structures

Numerical computer simulations are used to identify the details of defect splitting and local configurations of the LC between confining surfaces. These simulations are based on minimizing the Landau–de Gennes free-energy density f of a continuum representation of a LC, given by[71–73]

$$f = \frac{A}{2}Q_{ij}Q_{ji} + \frac{B}{3}Q_{ij}Q_{jk}Q_{ki} + \frac{C}{4}\left(Q_{ij}Q_{ji}\right)^2 + \frac{L_1}{2}\left(\frac{\partial Q_{ij}}{\partial x_k}\right)^2 + \frac{L_2}{2}\frac{\partial Q_{ij}}{\partial x_j}\frac{\partial Q_{ik}}{\partial x_k} + \frac{L_3}{2}\frac{\partial Q_{ij}}{\partial x_k}\frac{\partial Q_{ik}}{\partial x_j} + \frac{L_6}{2}Q_{ij}\frac{\partial Q_{kl}}{\partial x_i}\frac{\partial Q_{kl}}{\partial x_j} \quad (7)$$

with the summation over all indices assumed. The first three terms in the energy density with Landau expansion coefficients A, B and C describe the nematic–isotropic transition of the LC and quantifying the energy cost of singular defect cores, whereas the last four terms with spatial derivatives represent the elastic energy due to intermolecular interactions and reflect the energy penalty associated with distorting the LC director. The elasticity parameter $L_i, i = 1, 2, 3, 6$ can be related to the Frank–Oseen elastic constants of the nematic LC[73].

To model the splitting behaviour of line defects with high charges, the initial structures were constructed by assuming translationally invariant $\mathbf{n}(\mathbf{r})$ configurations along the vertical direction with the cross-section being the repeat unit of the designed vortex patterns and with constant value of the scalar order parameter. Dirichlet boundary conditions, corresponding to infinitely strong surface anchoring forces[61], were assumed at confining surfaces with the two-dimensional vortex patterns, whereas periodic boundary conditions were applied to the other dimensions. The numerical volume adopted an equidistant grid spacing in all dimensions, and the order parameter values were calculated and updated through a finite-difference method with an adaptive Runge–Kutta integration method of order three in each numerical iteration of the free-energy relaxation. The geometric dimensions and parameters were chosen to match our experimental values[74]. Computer simulations reproduced experimental results of split-core defect and field configurations (Fig. 3d,l), for surface boundary conditions with predesigned azimuthal angle patterns. Parameters used in our numerical modelling are provided in the Supplementary Information.

Simulation of polarizing optical micrographs

To directly compare the results of computer simulations with experiments, polarizing optical microscopy images are generated by utilizing the Jones-matrix approach[75,76]. First, the local Jones matrix of each grid point is calculated based on the director (optical axis) orientation and the ordinary/extraordinary phase retardation, defined by the optical anisotropy of the LC. Each pixel of the simulated image is then obtained by successive multiplication of Jones matrices across the light propagation direction. To approximate experimental images, the whole visible spectrum is represented by the combination of the red, green and blue colour wavelengths (640, 540 and 430 nm) with different light source intensities matching that of the experimental source. After a separate calculation for each wavelength, the three single-coloured images are combined to give the final computer-simulated image. Nematic mixture E7 with an optical anisotropy $\Delta n = 0.24$ is used in the modelling of the polarizing optical micrographs, which are found to closely match their experimental counterparts (Figs. 3 and 4).

Data availability

All data generated or analysed during this study are included in the published Article, and the material and geometric parameters used in Landau–de Gennes modelling as well as the details of sample preparation and nematicon excitation are provided in the Supplementary Information. Source data are provided with this paper.

Code availability

The codes used for Landau–de Gennes modelling and simulation of polarized optical micrographs are published in ref. [73]. The custom Lagrangian and Hamiltonion ray-tracing codes are provided in the Supplementary Information.

References

56. Meng, C., Tseng, M.-C., Tang, S.-T. & Kwok, H.-S. Optical rewritable liquid crystal displays without a front polarizer. *Opt. Lett.* **43**, 899–902 (2018).
57. White, T. J. & Broer, D. J. Programmable and adaptive mechanics with liquid crystal polymer networks and elastomers. *Nat. Mater.* **14**, 1087–1098 (2015).
58. Guo, D. Y. et al. Reconfiguration of three-dimensional liquid-crystalline photonic crystals by electrostriction. *Nat. Mater.* **19**, 94–101 (2020).
59. Tai, J.-S. B. & Smalyukh, I. I. Three-dimensional crystals of adaptive knots. *Science* **365**, 1449–1453 (2019).
60. Mundoor, H. et al. Electrostatically controlled surface boundary conditions in nematic liquid crystals and colloids. *Sci. Adv.* **5**, eaax4257 (2019).
61. Chigrinov, V. G., Kozenkov, V. M. & Kwok, H.-S. *Photoalignment of Liquid Crystalline Materials: Physics and Applications* (Wiley, 2008).
62. Subhash, H. M. Full-field and single-shot full-field optical coherence tomography: a novel technique for biomedical imaging applications. *Adv. Opt. Technol.* **2012**, 435408 (2012).
63. Ackerman, P. J. & Smalyukh, I. I. Diversity of knot solitons in liquid crystals manifested by linking of preimages in torons and hopfions. *Phys. Rev. X* **7**, 011006 (2017).
64. Martinez, A. et al. Mutually tangled colloidal knots and induced defect loops in nematic fields. *Nat. Mater.* **13**, 258–263 (2014).

65. Smalyukh, I. I., Lansac, Y., Clark, N. A. & Trivedi, R. P. Three-dimensional structure and multistable optical switching of triple-twisted particle-like excitations in anisotropic fluids. *Nat. Mater.* **9**, 139–145 (2010).
66. Varney, M. C., Jenness, N. J. & Smalyukh, I. I. Geometrically unrestricted, topologically constrained control of liquid crystal defects using simultaneous holonomic magnetic and holographic optical manipulation. *Phys. Rev. E* **89**, 022505 (2014).
67. Piccardi, A., Alberucci, A. & Assanto, G. Nematicons and their electro-optic control: light localization and signal readdressing via reorientation in liquid crystals. *Int. J. Mol. Sci.* **14**, 19932–19950 (2013).
68. Izdebskaya, Y. V., Desyatnikov, A. S., Assanto, G. & Kivshar, Y. S. Deflection of nematicons through interaction with dielectric particles. *J. Opt. Soc. Am. B* **30**, 1432–1437 (2013).
69. Joets, A. & Ribotta, R. A geometrical model for the propagation of rays in an anisotropic inhomogeneous medium. *Opt. Commun.* **107**, 200–204 (1994).
70. Poy, G. & Žumer, S. Ray-based optical visualisation of complex birefringent structures including energy transport. *Soft Matter* **15**, 3659–3670 (2019).
71. Hiroyuki, M., Gartland, E. C., Kelly, J. R. & Bos, P. J. Multidimensional director modeling using the Q tensor representation in a liquid crystal cell and its application to the π cell with patterned electrodes. *Jpn. J. Appl. Phys.* **38**, 135–146 (1999).
72. Ravnik, M. & Žumer, S. Landau–de Gennes modelling of nematic liquid crystal colloids. *Liq. Cryst.* **36**, 1201–1214 (2009).
73. Mundoor, H., Wu, J.-S., Wensink, H. H. & Smalyukh, I. I. Thermally reconfigurable monoclinic nematic colloidal fluids. *Nature* **590**, 268–274 (2021).
74. Klus, B., Laudyn, U. A., Karpierz, M. A. & Sahraoui, B. All-optical measurement of elastic constants in nematic liquid crystals. *Opt. Express* **22**, 30257 (2014).
75. Ackerman, P. J., Trivedi, R. P., Senyuk, B., van de Lagemaat, J. & Smalyukh, I. I. Two-dimensional skyrmions and other solitonic structures in confinement-frustrated chiral nematics. *Phys. Rev. E* **90**, 012505 (2014).
76. Ackerman, P. J., Boyle, T. & Smalyukh, I. I. Squirming motion of baby skyrmions in nematic fluids. *Nat. Commun.* **8**, 673 (2017).

Acknowledgements

We thank A. Hess, B. Li, H.-S. Kwok and T. Lee for discussions, as well as for providing technical assistance and materials. I.I.S. thanks the International Institute for Sustainability with Knotted Chiral Meta Matter with headquarters at Hiroshima University for hospitality during his stay in Japan, during which the initial version of this paper was written. Regarding funding, this research was supported by the US Department of Energy, Office of Basic Energy Sciences, Division of Materials Sciences and Engineering, under contract DE-SC0019293 with the University of Colorado at Boulder (C.M., J.-S.W. and I.I.S.). I.I.S. and C.M. also acknowledge the support of the US National Science Foundation (DMR-1810513) in the initial stages of this project.

Author contributions

C.M. prepared the photo-patterned samples and performed the experiments. J.-S.W. performed the theoretical analysis and numerical simulations of ray tracing and polarizing optical micrographs, with input from I.I.S.; C.M. and I.I.S. analysed data. I.I.S. conceived, designed and directed the research, provided funding and wrote the manuscript, with input from all authors.

Competing interests

The authors declare no competing interests.

Additional information

Extended data is available for this paper at https://doi.org/10.1038/s41563-022-01414-y.

Supplementary information The online version contains supplementary material available at https://doi.org/10.1038/s41563-022-01414-y.

Correspondence and requests for materials should be addressed to Ivan I. Smalyukh.

Peer review information *Nature Materials* thanks Ruth Durrer and the other, anonymous, reviewer(s) for their contribution to the peer review of this work.

https://doi.org/10.1038/s41563-022-01414-y

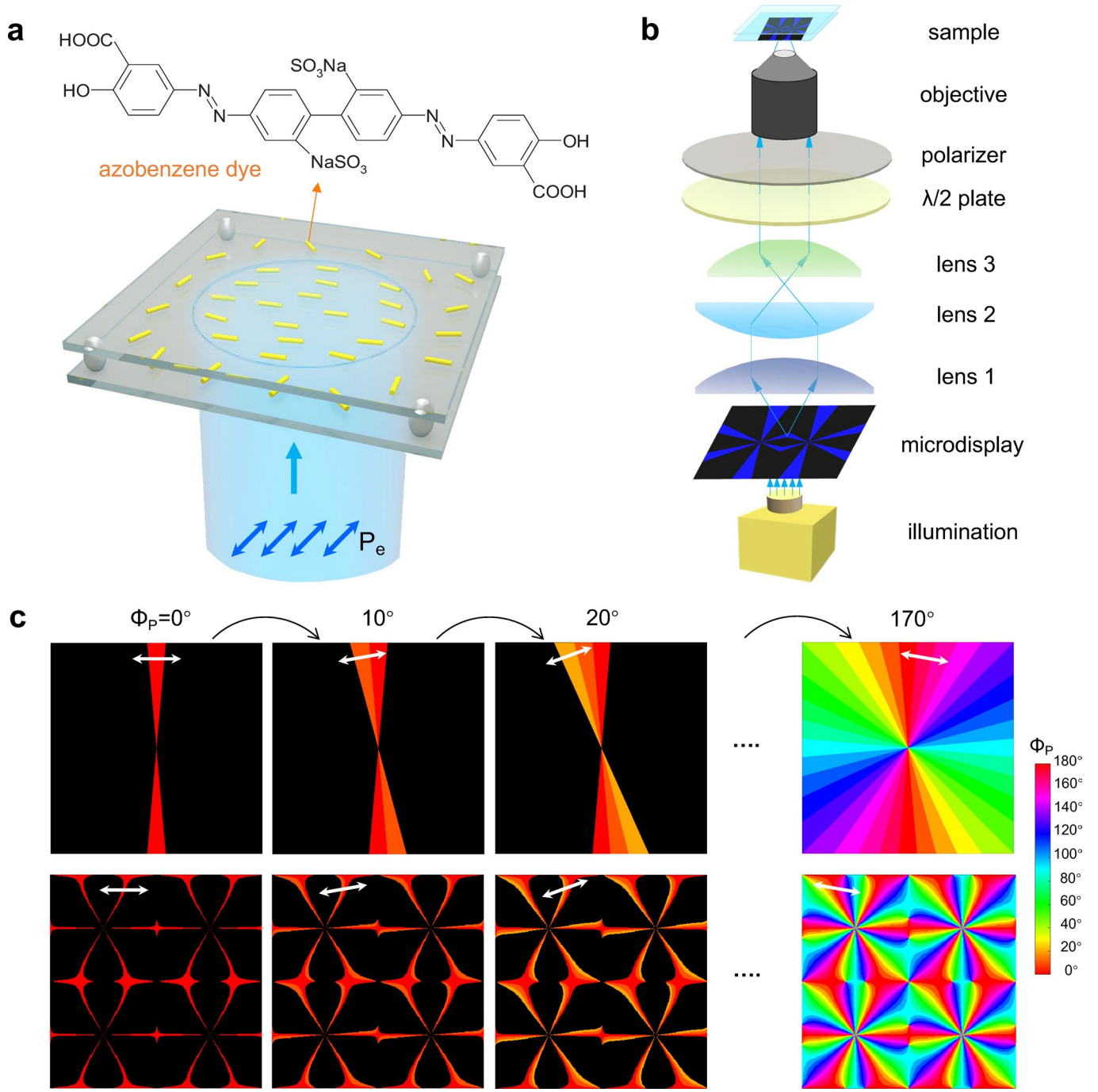

Extended Data Fig. 1 | Principles of photo-patterning of LC vortices. **a**, Optical response of azobenzene dye molecules to linearly polarized blue light, with the dye molecular structure shown above. When illuminated by the blue light, randomly oriented rodlike dye molecules collectively re-align to point orthogonally to the excitation light's polarization direction. **b**, Schematic setup of a custom-built photo-patterning system. The photo-patterning is based on a microdisplay used to project a computer-controlled blue-light pattern that is relayed by three lenses, linearly polarized by an inserted half-wave plate and a polarizer, and then projected to the back aperture of an objective, which focuses the pattern on the azobenzene dye layers. The pattern size is defined by the magnification of the objective. **c**, Vortices and their arrays are generated via sequential illuminations of patterns corresponding to narrow angular sectors of azimuthal orientations of dye molecules, synchronized with the corresponding control of the linear polarization (double white arrows) and its azimuthal orientation angle (Φ_p) to define dye molecule orientations at surfaces and, thus, define boundary conditions for $\mathbf{n}(\mathbf{r})$.

https://doi.org/10.1038/s41563-022-01414-y

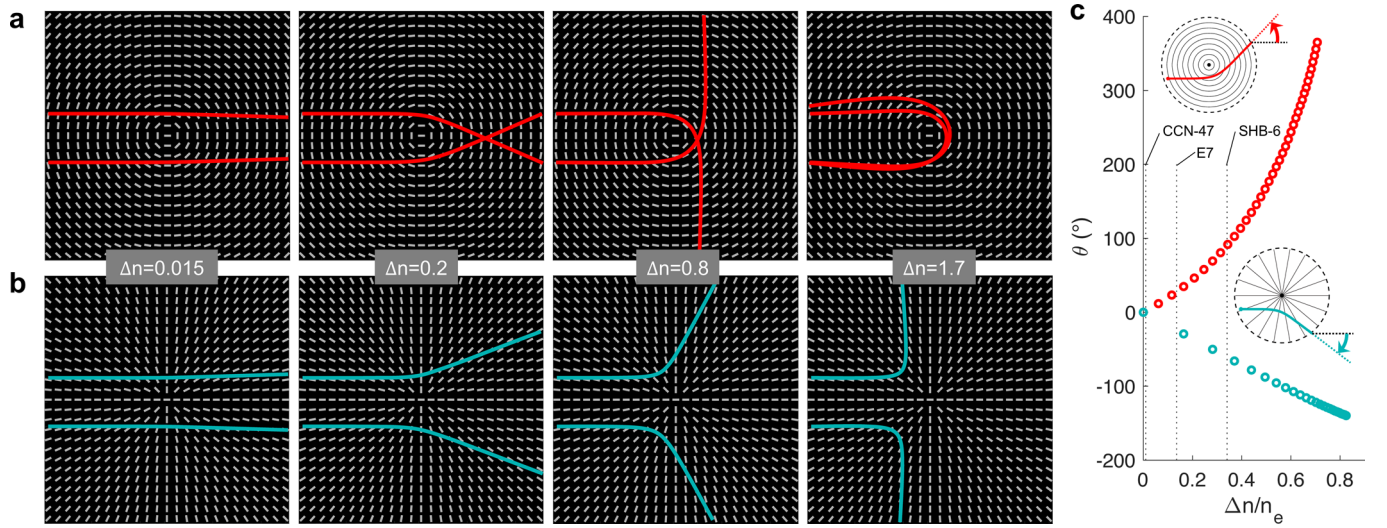

Extended Data Fig. 2 | Light steering in LCs with different Δ*n*. Numerically simulated optical trajectories (red/cyan lines) of light passing near the (**a**) $k = 1$, $\Psi_0 = \pi/2$ and (**b**) $k = 1$, $\Psi_0 = 0$ vortices formed within LCs with Δn of 0.015, 0.2, 0.8 and 1.7. The beams incident from the left side are initially parallel to the horizontal edges of the structures. White cylinders depict the spatial orientation of $\mathbf{n}(\mathbf{r})$. **c**, Numerically simulated deflection angle θ for such systems, with the value of θ being positive (negative) for deflection towards (away from) the center, as defined in the insets. Vertical dashed lines mark the material parameters for LCs including CCN-47 ($\Delta n = 0.015$), E7 ($\Delta n = 0.24$) and SHB-6 ($\Delta n = 0.79$). $n_o = 1.53$ for all simulations.

https://doi.org/10.1038/s41563-022-01414-y

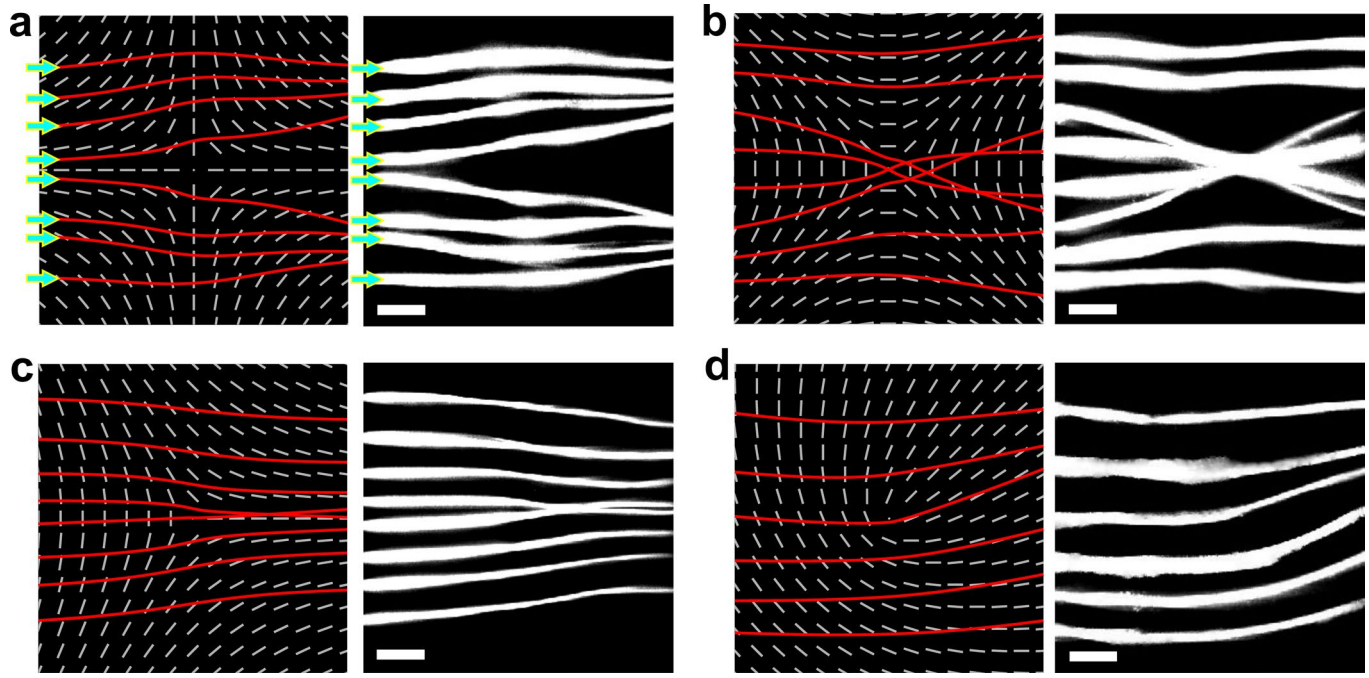

Extended Data Fig. 3 | Guiding of light by various topological vortices. **a**-**d**, (left) Computer-simulated light trajectories (red lines) overlaid atop of corresponding **n**(**r**) (white cylinders) and (right) experimental light propagation trajectories of 1064 nm laser beams emerging from different entry points (cyan arrows with yellow frame). The studied vortices from (**a**) to (**d**) are defects with: (**a**) $k = -1$, $\Psi_0 = 0$; (**b**) $k = -1$, $\Psi_0 = \pi/2$; (**c**) $k = -1/2$, $\Psi_0 = 0$ and (**d**) $k = 1/2$, $\Psi_0 = \pi/8$, respectively. The simulated beam trajectories are obtained using the Hamiltonian approach of ray tracing (Methods). All scale bars are 100 μm.

https://doi.org/10.1038/s41563-022-01414-y

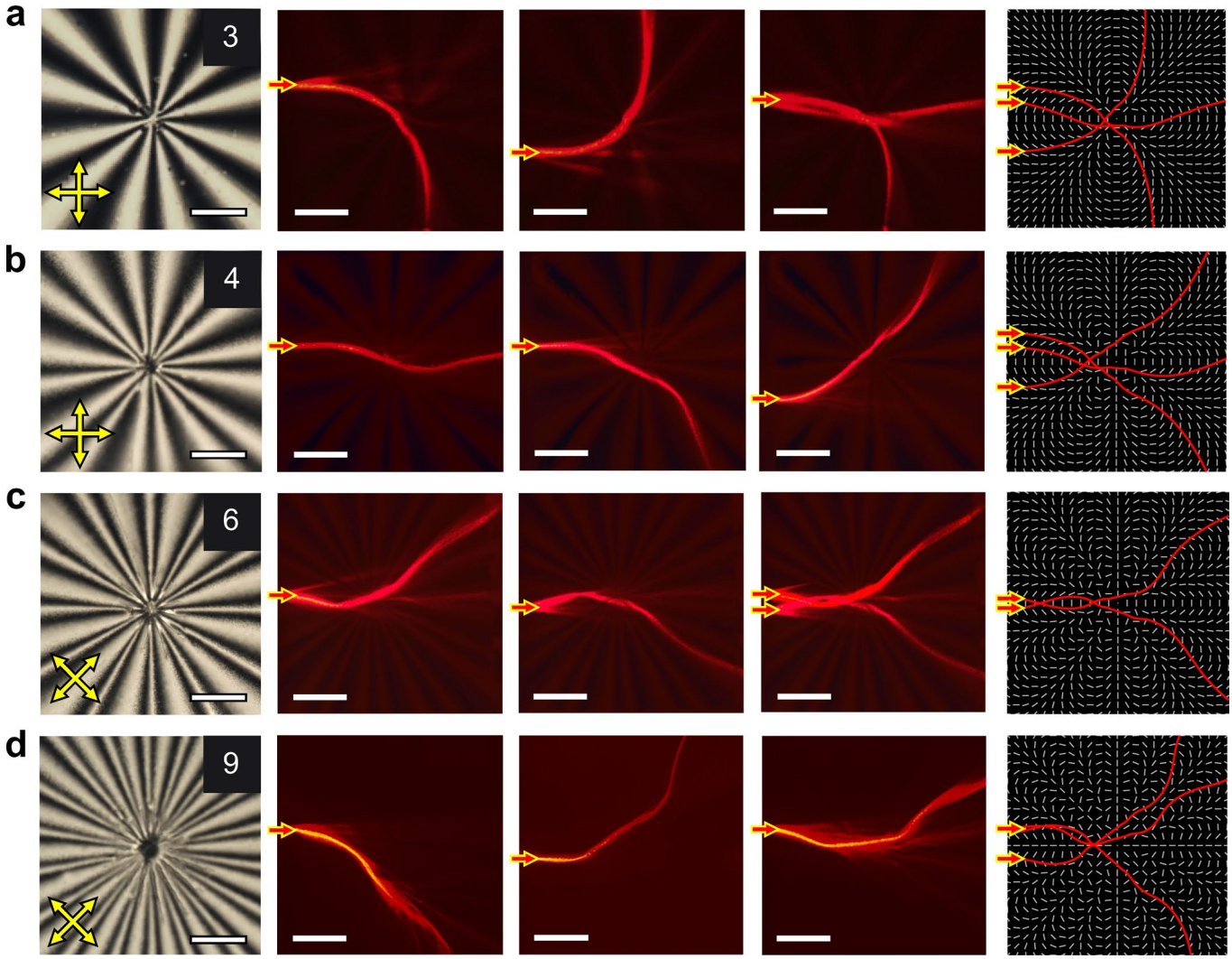

Extended Data Fig. 4 | Optical soliton steering by high-winding-number vortices. a-d, (left) Polarizing optical micrographs of vortices with winding numbers of $k = 3, 4, 6$ and 9 (marked on images) obtained between crossed polarizers (double yellow arrows). (3 middle panels) Experimental optical soliton trajectories for 650 nm laser beam launched at sites marked by red arrows with yellow frame, which closely match (right) computer-simulated trajectories plotted atop of associated $\mathbf{n}(\mathbf{r})$ (white cylinders). All scale bars are 100 μm.

https://doi.org/10.1038/s41563-022-01414-y

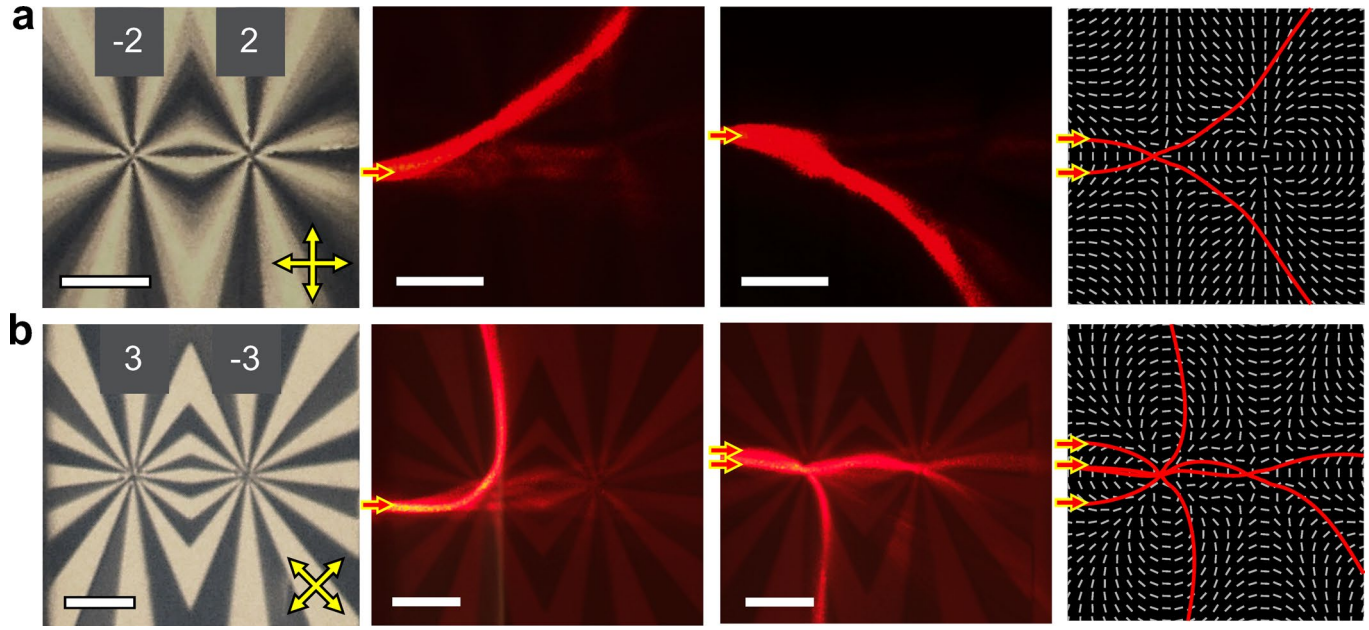

Extended Data Fig. 5 | Optical soliton steering by topological vortex dimers. **a**-**b**, (left) Polarizing optical micrographs of vortex dimers formed by vortices with (**a**) $k = -2$ and $k = 2$ and (**b**) $k = 3$ and $k = -3$, obtained under crossed polarizers (double yellow arrows). (2 middle panels) Optical soliton trajectories of 650 nm laser beam closely match (right) computer-simulated trajectories shown atop of the associated **n**(**r**) (white cylinders). All scale bars are 200 μm.

https://doi.org/10.1038/s41563-022-01414-y

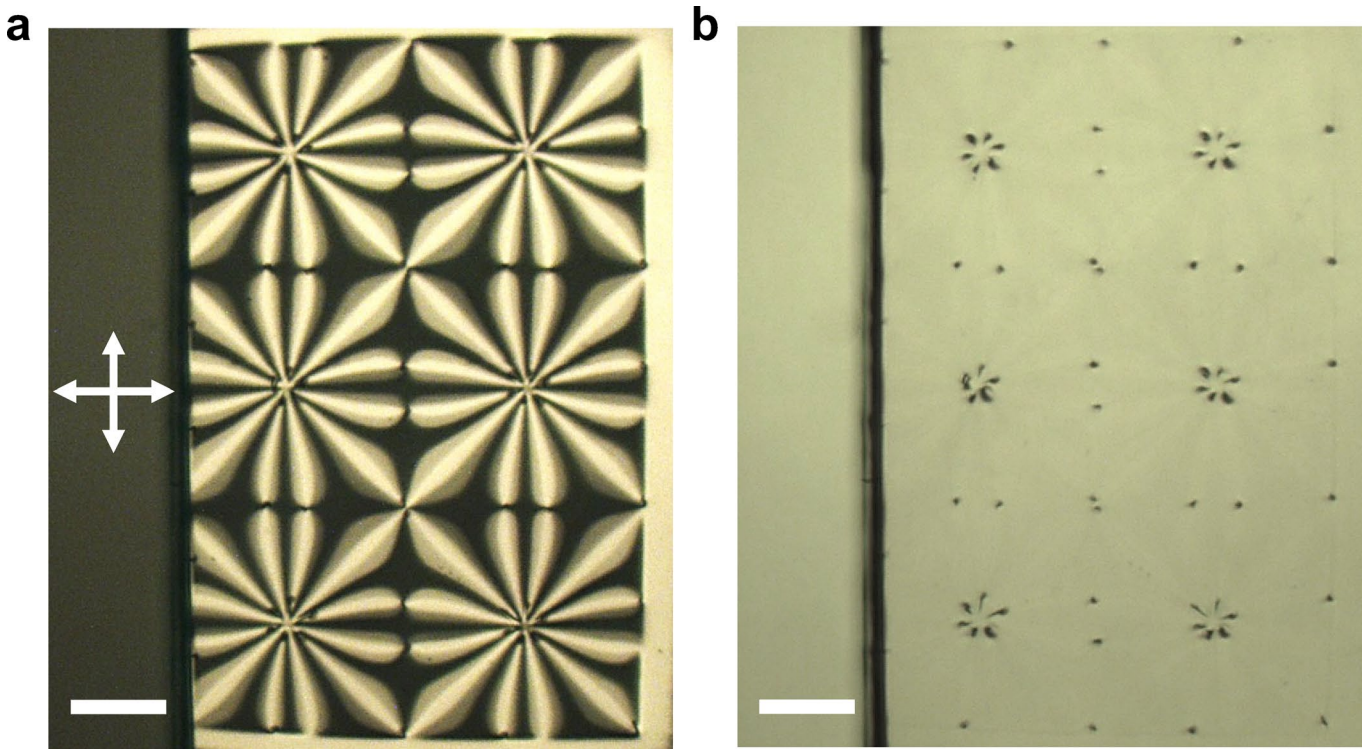

Extended Data Fig. 6 | Optical characterization of a vortex array. **a**-**b**, Polarizing (**a**) and brightfield (**b**) optical micrographs of a 3×2 array containing a vortex with $k = 3$, $\Psi_0 = 0$ surrounded by 12 bright and 12 dark brushes corresponding to 6π azimuthal **n**(**r**)-rotation in (**a**). The dark spots in (**b**) are half-integer defects to which cores of $k = 3$ (hexagons of dark spots) and $k = -1$ (pairs of dark spots) vortices split. Double white arrows mark orientations of crossed polarizers. Both scale bars are 200 μm.

https://doi.org/10.1038/s41563-022-01414-y

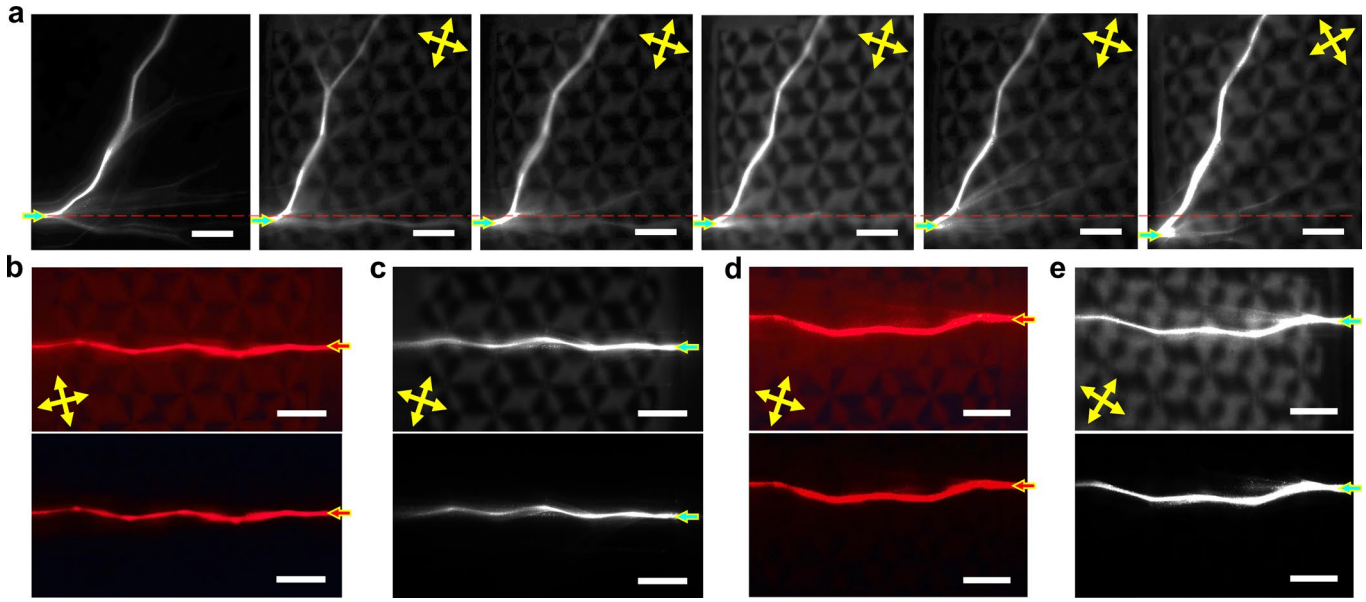

Extended Data Fig. 7 | Optical soliton propagation within arrays with $k = 1$ vortices. a, Lightning-like optical soliton propagations after slightly shifting 1064 nm laser beam with respect to the array. **b**-**e**, Meandering solitonic light trajectories generated by 650 nm (**b**,**d**) and 1064 nm (**c**,**e**) laser beams. The trajectories are captured (upper) with and (lower) without illumination backlight of the microscope. Double yellow arrows mark orientations of crossed polarizers. All scale bars are 200 μm.

https://doi.org/10.1038/s41563-022-01414-y

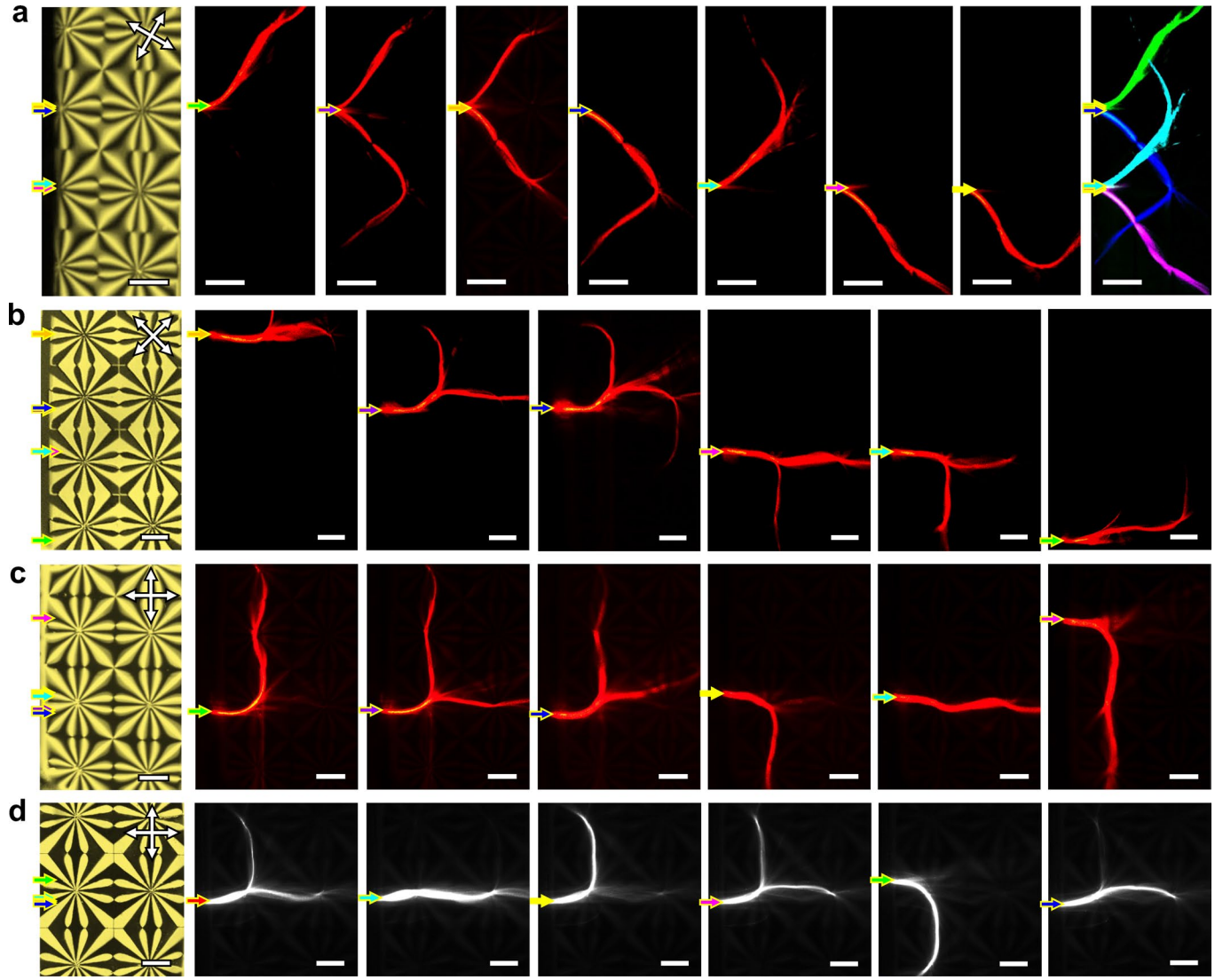

Extended Data Fig. 8 | Controlled fission of optical solitons. a-d, Interaction of light beams with arrays containing (**a**) $k = 3$, $\Psi_0 = \pi/2$ vortices and (**b-d**) $k = 3$, $\Psi_0 = 0$ vortices: (left panels) polarizing optical micrographs and (other panels) the corresponding experimental beam trajectories. Rightmost panel in (**a**) shows superposition of the individual light trajectories distinguished by false colours. All different soliton trajectories and fission events are obtained by slight shifting of the launching site of the beam, as marked by colored arrows with yellow frame. All scale bars are 200 μm, showing dimensions of the studied vortex arrays. The angular step of photo-patterning of vortex arrays is 11.25° in (**a**) 45° in (**b**,**d**) and 22.5° in (**c**).

https://doi.org/10.1038/s41563-022-01414-y

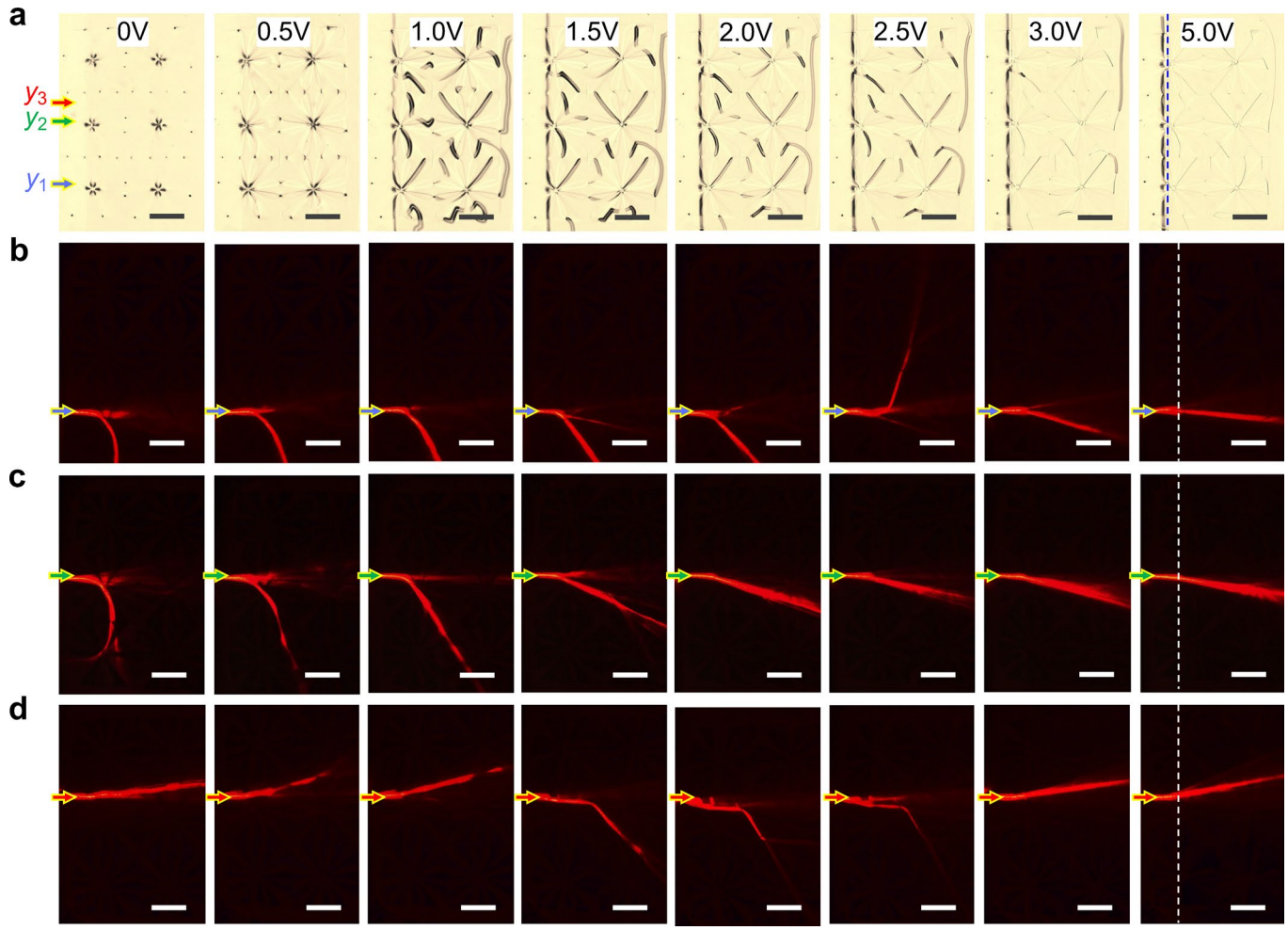

Extended Data Fig. 9 | Electric control of topological steering by an array with k = 3 vortices. a, Evolution of brightfield micrographs when applied voltage increases from 0 to 5.0 V, as marked on images. **b**-**d**, Light deflection trajectories at voltages corresponding to (**a**) when beams are launched from positions y_1, y_2 and y_3 marked in (**a**). Blue (**a**) and white (**b**-**d**) dashed lines mark the edge of indium tin oxide electrodes, with the right-side of the sample having the electrode and being responsive to applied voltage. All scale bars are 200 μm.

https://doi.org/10.1038/s41563-022-01414-y

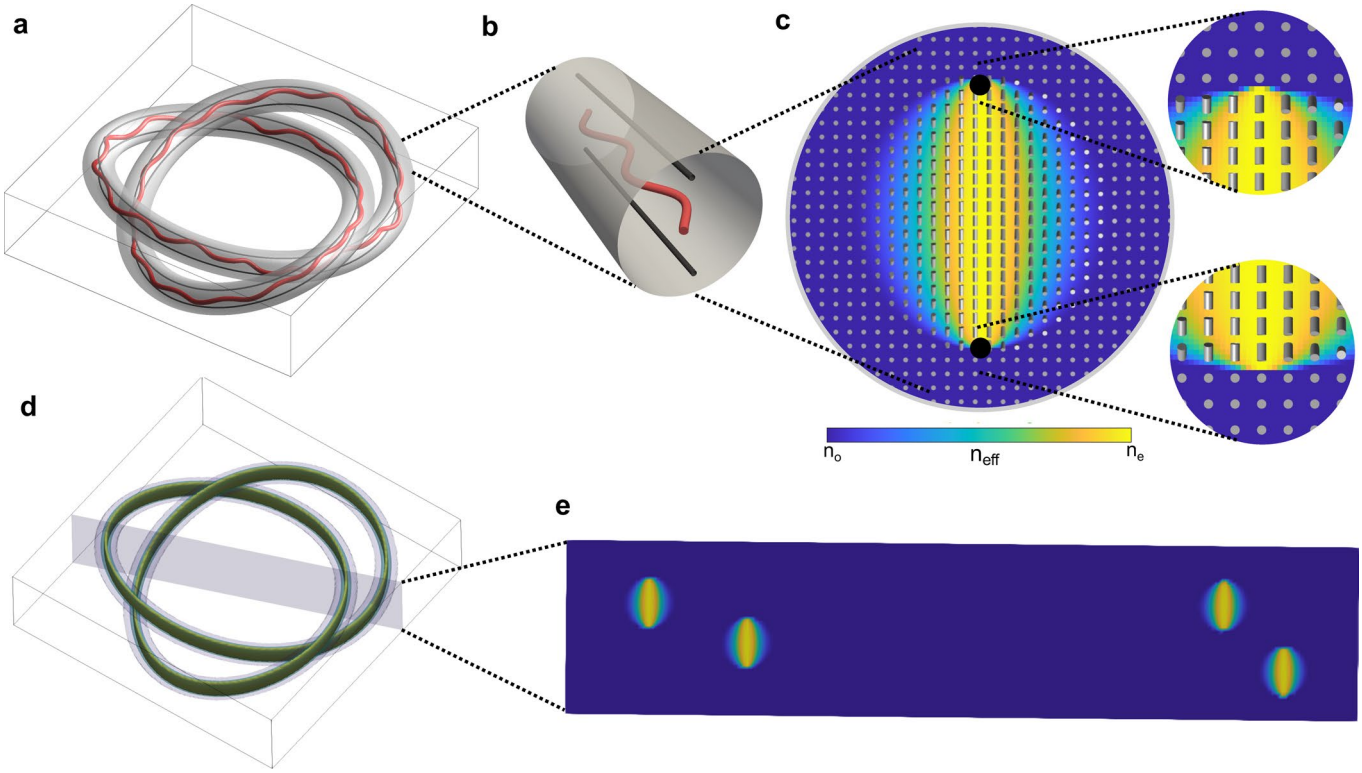

Extended Data Fig. 10 | Engineering knots of light beams with the help of knotted vortices. a, Waveguiding of a light beam (red line) in a high-index knotted region defined by a pair of trefoil-knot-shaped loops of vortices (black lines). **b**, A zoom-in view of the tube-like high-index region forming the trefoil knot shown in (**a**). **c**, A detailed view of the director structure and refractive index distribution within a cross-section of the knotted tubelike region, where the right-side insets show details of director rotations around the vortex lines and the bottom inset provides the colour scheme for the refractive index varying between the ordinary and extraordinary values. **d**, The three-dimensional distribution of the refractive index variation and **e**, its corresponding variation in a cross-sectional plane depicted in (**d**), with the high-index regions corresponding to intersections of the knotlike high-index structure with the plane, as clearly seen. Once coupled to such a knot-shaped topological waveguide, light would be confined to propagate within the knot.